























# The Relative Impact of Astrophysics and Halo-to-Halo Variation on the Dark Matter Density Profiles of Milky Way-Mass Halos

ALEX M. GARCIA <sup>1, 2, 3</sup> JONAH C. ROSE <sup>4, 5</sup> PAUL TORREY <sup>1, 2, 3</sup> ANDREA CAPUTO <sup>6, 7</sup>  
MARIANGELA LISANTI <sup>4, 5</sup> ANDREW B. PACE <sup>1</sup> HONGWAN LIU <sup>8</sup> ABDELAZIZ HUSSEIN <sup>9</sup> HAOZHE LIU,<sup>1</sup>  
FRANCISCO VILLAESCUSA-NAVARRO <sup>5</sup> JOHN BARRY,<sup>10</sup> ILEM LEISHER <sup>11, 12, 13</sup> BELÉN COSTANZA <sup>14, 15</sup>  
JONATHAN KHO <sup>1, 2, 3</sup> ETHAN LILLE <sup>4</sup> JIAXUAN LI (李嘉轩) <sup>16</sup> NIUSHA AHVAZI <sup>1, 2, 3</sup> TRI NGUYEN <sup>17, 18</sup>  
STEPHANIE O'NEIL <sup>19, 4</sup> XIAOWEI OU <sup>1, 2, 3</sup> XUEJIAN SHEN <sup>9</sup> NITYA KALLIVAYALIL <sup>1, 3</sup> LINA NECIB <sup>9, 20</sup> AND  
MARK VOGELSBERGER <sup>9, 20</sup>

<sup>1</sup>Department of Astronomy, University of Virginia, 530 McCormick Road, Charlottesville, VA 22904

<sup>2</sup>Virginia Institute for Theoretical Astronomy, University of Virginia, Charlottesville, VA 22904, USA

<sup>3</sup>The NSF-Simons AI Institute for Cosmic Origins, USA

<sup>4</sup>Department of Physics, Princeton University, Princeton, NJ 08544, USA

<sup>5</sup>Center for Computational Astrophysics, Flatiron Institute, 162 5th Avenue, New York, NY 10010, USA

<sup>6</sup>Theoretical Physics Department, CERN, 1211 Geneva 23, Switzerland

<sup>7</sup>Dipartimento di Fisica, “Sapienza” Università di Roma, Italy & Sezione INFN Roma1, Piazzale Aldo Moro 5, 00185, Roma, Italy

<sup>8</sup>Physics Department, Boston University, Boston, MA 02215, USA

<sup>9</sup>Department of Physics and Kavli Institute for Astrophysics and Space Research, Massachusetts Institute of Technology, Cambridge, MA 02139, USA

<sup>10</sup>College of Science at Northeastern University, 360 Huntington Avenue, 115 Richards Hall, Boston, MA 02115

<sup>11</sup>Grinnell College, 1115 8th Ave, Grinnell, IA 50112, USA

<sup>12</sup>Department of Physics, Massachusetts Institute of Technology, Cambridge, MA 02139, USA

<sup>13</sup>Kavli Institute for Astrophysics and Space Research, Massachusetts Institute of Technology, Cambridge, MA 02139, USA

<sup>14</sup>Facultad de Ciencias Astronómicas y Geofísicas, Universidad Nacional de La Plata, Observatorio Astronómico, Paseo del Bosque, B1900FWA La Plata, Argentina

<sup>15</sup>Consejo Nacional de Investigaciones Científicas y Técnicas (CONICET), Rivadavia 1917, Buenos Aires, Argentina

<sup>16</sup>Department of Astrophysical Sciences, 4 Ivy Lane, Princeton University, Princeton, NJ 08540, USA

<sup>17</sup>Center for Interdisciplinary Exploration and Research in Astrophysics, Northwestern University, 1800 Sherman Ave, Evanston, IL 60201

<sup>18</sup>NSF-Simons AI Institute for the Sky, 172 E. Chestnut St., Chicago, IL 60611, USA

<sup>19</sup>Department of Physics & Astronomy, University of Pennsylvania, Philadelphia, PA 19104, USA

<sup>20</sup>The NSF AI Institute for Artificial Intelligence and Fundamental Interactions, Cambridge, MA 02139, USA

## ABSTRACT

Experimental searches for dark matter require reliable models of the Milky Way’s density, which in turn depend on understanding the influence of baryonic feedback. In this work, we utilize a new suite of Milky Way mass halos simulated with Cold Dark Matter (CDM) from the DREAMS Project to quantify the influence of baryon feedback and intrinsic halo-to-halo variance on dark matter density profiles. Our suite of 1024 halos (a factor of approximately five more than current cosmological volumes at similar resolution) varies over supernova and black hole feedback parameters from the IllustrisTNG model, as well as variations in two cosmological parameters,  $\Omega_M$  and  $\sigma_8$ . We find that Milky Way-mass dark matter density profiles in the IllustrisTNG model are largely insensitive to astrophysics and cosmology variations, with the dominant source of scatter instead arising from halo-to-halo variance. However, most of the (comparatively minor) feedback-driven variations come from the changes to supernova prescriptions. By comparing to dark matter only simulations, we find that the strongest supernova wind energies are so effective at preventing galaxy formation that the halos are nearly entirely collisionless dark matter. Finally, regardless of physics variation, all the DREAMS halos are roughly consistent with a halo contracting adiabatically from the presence of baryons, unlike models that have bursty stellar feedback. This work represents a step toward assessing the robustness of

Milky Way dark matter profiles, with direct implications for dark matter searches, where systematic uncertainty in the density profile remains a major challenge.

## 1. INTRODUCTION

Baryons make up only a small fraction of the total mass budget of the Universe (Planck Collaboration et al. 2016), yet they play a central role in driving galaxy evolution. Unlike the dark matter component, which is assumed to be cold and collisionless in the standard Cold Dark Matter (CDM) model, the baryonic component experiences interactive forces and energy dissipation. These interactions ultimately facilitate the condensation of gas at the centers of halos and the formation of the galaxies we observe (Fall & Efstathiou 1980; Blumenthal et al. 1986). Once a galaxy is formed, baryons can impart feedback in their environments through various forms of stellar and black hole feedback including supernovae, stellar winds, and active galactic nuclei (AGN) activity (e.g., Dekel & Silk 1986; Larson 1974; Somerville & Davé 2015). Through interactions, dissipation, and feedback, baryons drive time-varying changes in the gravitational potential that shape galaxy evolution.

The role that baryons play can be clearly seen in the distribution of matter within a halo. Early dark matter-only (DMO) simulations showed that dark matter halos ubiquitously form a two-component power-law density profile known as the Navarro, Frenk, & White (1997; NFW) profile such that

$$\rho(r) = \frac{\rho_s}{\left(\frac{r}{r_s}\right) \left[1 + \left(\frac{r}{r_s}\right)\right]^2}, \quad (1)$$

where  $\rho_s$  is the scale density and  $r_s$  is the scale radius of the profile. Interior to the scale radius, the NFW profile has a power-law index of  $-1$  which then transitions beyond the scale radius to a power-law with an index of  $-3$ . From an observational perspective, measurements of galactic rotation curves provide constraints for the distribution of the mass within a halo (Rubin et al. 1980; Persic et al. 1996; Sofue & Rubin 2001; Huang et al. 2016; Zhang et al. 2024). These observations show that, while massive halos (e.g., clusters,  $\sim 10^{14} M_\odot$ ) tend to be roughly consistent with the NFW inner power-law index of  $\sim 1$  (e.g., Newman et al. 2013), observed dwarf galaxies ( $\sim 10^9\text{--}10^{10} M_\odot$ ) often have “cored” (inner power-law  $\ll 1$ ) density profiles (de Blok & Bosma 2002; de Blok et al. 2008; Walker & Peñarrubia 2011). Moreover, at intermediate scales, Milky Way-mass halos ( $\sim 10^{12} M_\odot$ ) can exhibit a wide range of inner density slopes and rotation curve shapes (e.g., Oman et al. 2015; Ou et al. 2024, 2025). The striking

diversity of density profiles contrasts with the relatively uniform predictions of dark-matter-only simulations, a discrepancy known as the diversity problem (e.g., Oman et al. 2015; Bullock & Boylan-Kolchin 2017), a generalization of the core-cusp problem (de Blok 2010).

Simulations which self-consistently model the baryonic component provide one possible resolution to these tensions (Sales et al. 2022). A cored inner density can be achieved using sufficiently “bursty” supernova feedback (Chan et al. 2015; Lazar et al. 2020; Mostow et al. 2024). Repetitively cycling between slow/smooth inflows followed by fast/impulsive outflows creates central potential fluctuations that disrupt the orbits of dark matter particles and lead to decreased central densities (Governato et al. 2010; Pontzen & Governato 2012; Oñorbe et al. 2015; Jahn et al. 2023). However, even at fixed physics prescriptions, the diversity of halo assembly histories introduces substantial halo-to-halo variance in the resulting dark matter profiles (e.g., Abadi et al. 2010; Duffy et al. 2010; Di Cintio et al. 2014; Chan et al. 2015; Fitts et al. 2017; Lazar et al. 2020). Disentangling this intrinsic variance from systematic shifts due to baryonic physics is therefore critical for interpreting both simulations and observations. Moreover, the level to which feedback is generically bursty and its evolutionary consequences across different galaxy populations remains uncertain (see, e.g., work by Hartley & Ricotti 2016; Bhagwat et al. 2024; Garcia et al. 2023, 2024a,b, 2025a,b).

Current cosmological simulations of galaxy evolution follow several prescriptions for modeling the physics of baryons (see, e.g., Vogelsberger et al. 2020; Crain & van de Voort 2023; Feldmann & Bieri 2025, for reviews). These prescriptions often rely on “subgrid” models for the numerical implementations of unresolved physics. For example, the interstellar medium (ISM) is often treated with an effective equation of state that sets the behavior of dense ( $n_H \gtrsim 0.1 \text{ cm}^{-3}$ ) star forming gas (Springel & Hernquist 2003; Schaye & Dalla Vecchia 2008). Subgrid models require assumptions and oftentimes contain tunable parameters within the model. As a result, different simulation models make different predictions for the role of baryons and their associated feedback—even with relatively similar implementations (e.g., Chua et al. 2019, 2022; Garcia et al. 2024a, 2025a,b). Some work has been done to this point to quantify the variation in model predictions based on the input physics (e.g., Duffy et al. 2010; Torrey et al. 2014; Pillepich et al. 2018a; Chua et al. 2019,

2022; Font et al. 2020; Kugel et al. 2023), but the number of model variations is usually few (on the order of  $\sim 10$ s of model variations). Recent simulation efforts with the CAMELS (Villaescusa-Navarro et al. 2021; Ni et al. 2023) and DREAMS (Rose et al. 2025) suites have begun to more systematically explore the parameter space of well-tested simulation models via thousands of model variations. These efforts allow for quantification of the detailed role parameter while also providing large enough samples to begin quantifying the intrinsic halo-to-halo variance.

One model that departs sharply from the standard approach is FIRE (Hopkins et al. 2014, 2018), which explicitly resolves the multiphase interstellar medium. While FIRE does not resolve everything in galaxies and has its own subgrid assumptions and parameters, the treatment of the star forming interstellar medium (ISM) is a marked improvement compared to the standard approach of an effective equation of state. One feature of the FIRE model is the production of strong, time-variable stellar feedback-driven winds (i.e., bursty feedback; Muratov et al. 2015), whereas models that adopt treatment yield smoother, less variable stellar feedback. In the absence of this bursty feedback, the evolution of a dark matter halo is governed by the response of the dark matter to the baryons cooling to the center. This adiabatic contraction can be modeled via the conservation of action integrals (e.g., Eggen et al. 1962; Blumenthal et al. 1986; Gnedin et al. 2004; Cautun et al. 2020): as the potential deepens due to baryon mass accumulation, the radius of the dark matter orbits decreases causing the total density in the center to increase. Feedback can partially offset or even reverse this contraction, but the degree depends sensitively on feedback (Brooks & Zolotov 2014; Lovell et al. 2018; Hussein et al. 2025). Indeed, Hussein et al. (2025) show that FIRE-2 galaxies deviate much more from adiabatic contraction than simulations with equation of state ISM prescriptions, though it remains unclear whether this owes specifically to burstiness or just the overall feedback strength.

In this work, we employ the new DREAMS CDM suite of Milky Way-mass halos to quantify the role of variations to the IllustrisTNG physics model on the dark matter density profiles of halos. The novelty of this DREAMS suite is that it contains 1024 Milky Way-mass halos, a factor of five more than the TNG volume at comparable resolution, as well as systematic variations in our baryonic feedback prescriptions. Crucially, the large number of halos also allows us to quantify the contribution of halo-to-halo variance, and to compare its relative importance to the impact of physics variations. The rest of this paper is organized as follows.

In Section 2, we introduce the DREAMS simulations, their parameter variations, and halo selection. We then outline our method for reconstructing dark matter density fields, describe the neural network emulators used in this work, and discuss a scheme to account for how well our halos match observed galaxy scaling relations. In Section 3, we discuss the dark matter density profiles and fit them with an analytic function. In Section 4, we compare the hydro simulations to DMO simulations, quantify the contraction the halos must have undergone due to the presence of baryons, and contrast our results to those from the bursty feedback FIRE model. Finally, in Section 5, we state our conclusions.

## 2. METHODS

### 2.1. DREAMS Simulations

This work makes use of data products from the DREAMS suites of simulations (Rose et al. 2025).<sup>1</sup> In particular, we use the zoom-in simulations from the Cold Dark Matter (CDM) suite (Rose et al. (Centrals)).<sup>2</sup> Each target halo falls within the mass range  $5.8 \times 10^{11} M_{\odot} < M_{\text{Halo}} < 2.0 \times 10^{12} M_{\odot}$ , roughly corresponding to the mass of the Milky Way halo (Callingham et al. 2019; Wang et al. 2020), where  $M_{\text{Halo}}$  is the sum of all mass within  $R_{200}$  (Springel et al. 2005). There are a total of 2048 simulations in the DREAMS Milky Way CDM suite: 1024 DMO simulations as well as a corresponding pair of 1024 simulations with baryon physics included. Each pair has the same initial conditions, such that the same halo is simulated twice.

The hydrodynamic simulations are based on the IllustrisTNG (hereafter simply TNG) physics model (Marinacci et al. 2018; Naiman et al. 2018; Nelson et al. 2018; Pillepich et al. 2018b; Springel et al. 2018; Pillepich et al. 2019; Nelson et al. 2019a,b). TNG is built on the moving Voronoi mesh code AREPO (Springel 2010a). The TNG model implements a wide range of astrophysical processes including (but not limited to) feedback from stars, the growth of supermassive black holes, feedback from active galactic nuclei (AGN), cosmological expansion of the universe, gravity, dark matter, and galactic winds (we refer the reader to Pillepich et al. 2018a, for a complete description of the TNG model).

The DREAMS halos are selected using an iterative zoom-in process (described in detail in Rose et al. 2025, Rose et al. Centrals). Briefly, the halos are selected

<sup>1</sup> [dreams-project.org](https://dreams-project.org)

<sup>2</sup> We also explore the Warm Dark Matter (WDM) suite of Milky Way-mass halos (Rose et al. 2025) in Appendix B; however, we find no systematic trends in the density profiles with WDM particle mass.



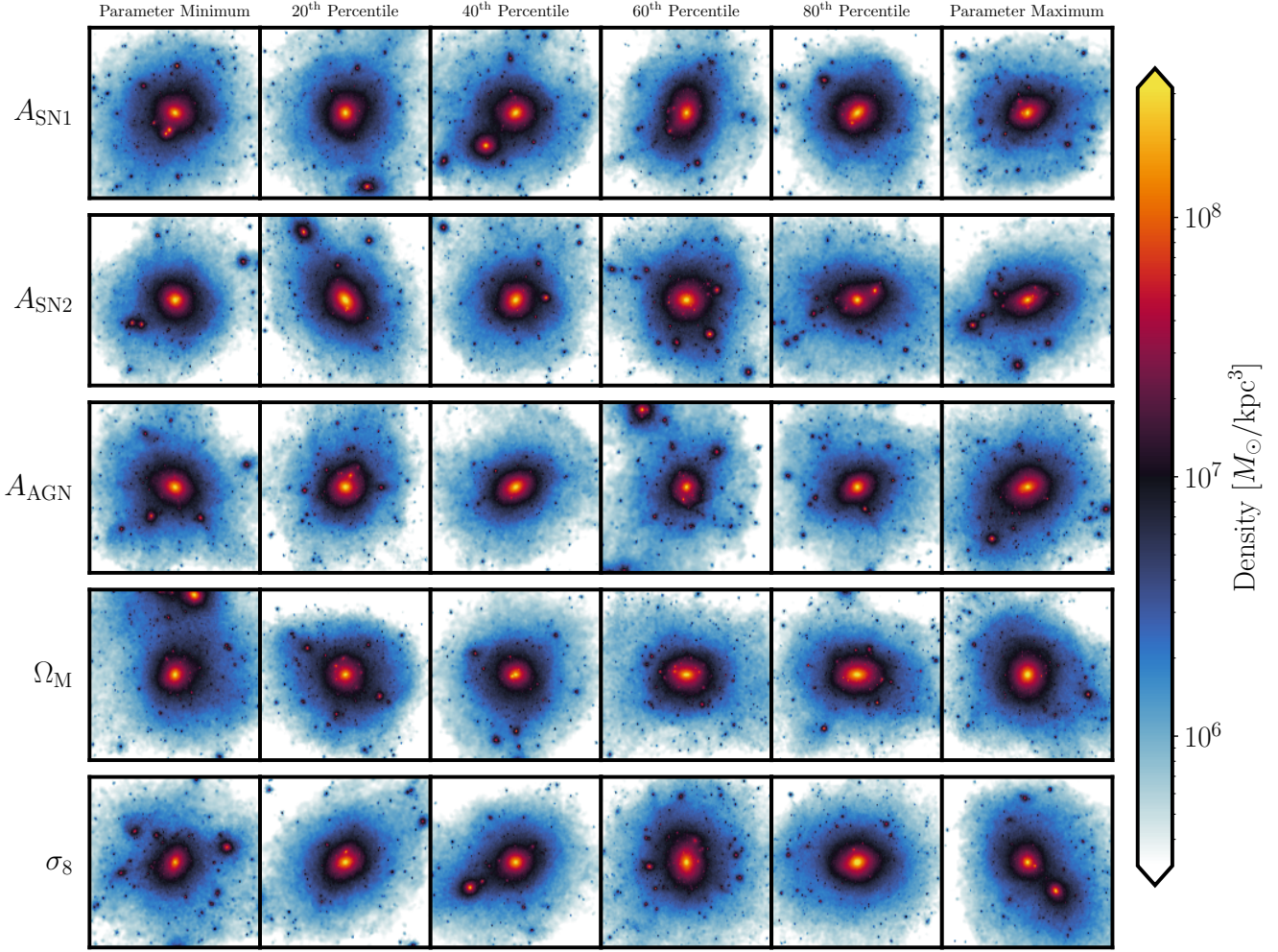


**Figure 1. Milky Way Mass Dark Matter Halos from the SB5 DREAMS CDM Suite.** Projections of the dark matter density of a small fraction ( $\sim 3\%$ ) of DREAMS halos within their  $R_{200}$ . Each row contains variations of the five DREAMS parameters ( $A_{\text{SN1}}$ ,  $A_{\text{SN2}}$ ,  $A_{\text{AGN}}$ ,  $\Omega_{\text{M}}$ , and  $\sigma_8$ , top-to-bottom, respectively; see Table 1 and Section 2.1.1). Each column represents the minimum, 20<sup>th</sup> percentile, 40<sup>th</sup> percentile, 60<sup>th</sup> percentile, 80<sup>th</sup> percentile, and maximum variation of each parameter (left-to-right, respectively). We note that the simulations are not strictly one parameter variations. Moreover, the halos simulated here are all generated using different initial conditions (see Rose et al. 2025). Thus, these simulations capture: (i) the variance due to single parameters, (ii) the co-variance between different parameters, and (iii) halo-to-halo variation.

Parameter	Brief Description	Fiducial TNG Value	Variations
$A_{\text{SN1}}$	SN Wind Energy	3.6	$[0.25-4] \times 3.6$
$A_{\text{SN2}}$	SN Wind Speed	7.4	$[0.5-2] \times 7.4$
$A_{\text{AGN}}$	AGN Feedback Strength	0.1	$[0.25-4] \times 0.1$
$\Omega_{\text{M}}$	Matter Density of Universe	0.31	$[0.274-0.354]$
$\sigma_8$	Amplitude of Matter Clustering on 8 Mpc Scales	0.8159	$[0.780-0.888]$

**Table 1. Astrophysical and Cosmological Parameter Variations.** The astrophysical ( $A_{\text{SN1}}$ ,  $A_{\text{SN2}}$ ,  $A_{\text{AGN}}$ ) and cosmological ( $\Omega_{\text{M}}$ ,  $\sigma_8$ ) parameters varied in the CDM DREAMS Milky Way-mass zoom-in simulations. We list the fiducial TNG value for each parameter, the variations used in these simulations (corresponding to a factor of 4 for  $A_{\text{SN1}}$  and  $A_{\text{AGN}}$ , a factor of 2 for  $A_{\text{SN2}}$ , and the two-standard-deviation uncertainty on Planck Collaboration et al. 2014 for  $\Omega_{\text{M}}$  and  $\sigma_8$ ). We sample the unique set of parameters for each simulation according to a Sobol’ (1967) sequence. Finally, we note that  $A_{\text{SN1}}$ ,  $A_{\text{SN2}}$ , and  $A_{\text{AGN}}$  are sampled in logarithmic space, whereas  $\Omega_{\text{M}}$  and  $\sigma_8$  are sampled in linear space. Detailed justifications for these parameter ranges can be found in Rose et al. (2025).

initially from a low-resolution  $(100 \text{ Mpc}/h)^3$  DMO simulation, which are then resimulated with DMO zooms. The target halos of the intermediate zooms are selected to have masses of  $7 \times 10^{11} \text{ M}_\odot < M_{\text{Halo}} < 2.0 \times 10^{12} \text{ M}_\odot$  and no massive ( $M_{\text{Halo}} > 5 \times 10^{11} \text{ M}_\odot$ ) galaxy within 1 Mpc at  $z=0$ . These zoom-in systems are then resimulated with hydrodynamics and baryonic feedback turned on by increasing the resolution of all particles within  $5R_{200}$ .

The key advantage of the DREAMS simulations is that they contain wide and systematic variations over the fiducial TNG astrophysical ( $A_{\text{SN1}}$ ,  $A_{\text{SN2}}$ , and  $A_{\text{AGN}}$ ) and cosmological parameters ( $\Omega_{\text{M}}$  and  $\sigma_8$ ), as well as a range of initial conditions that sample rare environments and formation histories. The simulation parameters are varied according to a Sobol’ (1967) sequence where each simulation represents its own unique realization of TNG physics and cosmology (i.e., SB5 or “Sobol 5” in the parlance of the CAMELS simulations; Villaescusa-Navarro et al. 2021). Detailed motivation for the parameter ranges can be found in Rose et al. (2025, their Section 2.1). In the following two subsections, we define each of the varied parameters as well as their ranges, as summarized in Table 1. Aside from the two cosmological parameters explicitly varied, the rest of the cosmology in DREAMS is fully consistent with Planck Collaboration et al. (2016):  $\Omega_{\Lambda} = 0.698$ ,  $H_0 = 100h \text{ km s}^{-1} \text{ Mpc}^{-1}$  where  $h = 0.6909$ , and  $\Omega_b = 0.046$ .

The dark matter mass resolution of the both the hydro and DMO simulations is implicitly varied by the variations in  $\Omega_{\text{M}}$  – the matter density of the universe. The dark matter mass resolution in the hydro simulations is  $1.8 \times (\Omega_{\text{M}} / 0.314) \times 10^6 \text{ M}_\odot$ , while the baryon mass resolution is  $2.8 \times 10^5 \text{ M}_\odot$  (with the baryon mass resolution being approximately a factor of two coarser resolution than the TNG50 suite; Pillepich et al. 2019). Importantly, the DMO simulations are generated with a baryon density of  $\Omega_b = 0.046$  to preserve baryon acoustic oscillations, but the baryon particles are treated as collisionless. In other words, the dark matter particles in the DMO simulations are more massive by a factor of  $(\Omega_b - \Omega_{\text{M}})/\Omega_{\text{M}}$ . All other numerical parameters (e.g., softening lengths) are the same between the two sets of simulations.

### 2.1.1. Parameter Variations

There are three astrophysical parameters— $A_{\text{SN1}}$ ,  $A_{\text{SN2}}$ , and  $A_{\text{AGN}}$ —that are varied in every DREAMS simulation. Both  $A_{\text{SN1}}$  and  $A_{\text{SN2}}$  relate to the feedback from stars in the TNG model whereas  $A_{\text{AGN}}$  relates to the feedback from supermassive black holes.

Given the limited mass resolution of TNG, feedback from stars is necessarily treated on a ‘subgrid’ level. This subgrid prescription accounts for the ejection of winds from unresolved supernovae explosions. This feedback is primarily governed in the TNG model by the mass-loading factor of winds generated by the supernovae. The mass-loading factors in TNG are given by the expression

$$\eta_w = \frac{2}{v_w^2} e_w (1 - \tau_w) . \quad (2)$$

There are three free parameters in Equation 2 that decide the strength of feedback: specific energy of the winds ( $e_w$ ), the wind velocity ( $v_w$ ), and the fraction of thermal energy that is released ( $\tau_w$ ). The DREAMS simulations vary both the energy and speed of the winds while keeping the fraction of thermal energy constant to its fiducial TNG value ( $\tau_w = 0.1$ ).

The specific energy is defined such that

$$e_w = A_{\text{SN1}} \cdot f(Z) \cdot N_{\text{SN}} \left[ 10^{51} \frac{\text{erg}}{\text{M}_\odot} \right] , \quad (3)$$

where  $A_{\text{SN1}}$  is a dimensionless scaling on the energy per supernova,  $f(Z)$  is a function that reduces that available energy when the metallicity ( $Z$ ) is above a reference value, and  $N_{\text{SN}}$  is the number of Type II supernovae.  $N_{\text{SN}}$  depends both on the shape and mass limits of the assumed initial mass function (IMF): both TNG and DREAMS assume a Chabrier (2003) IMF with a minimum core-collapse supernova mass of  $8 \text{ M}_\odot$ . The fiducial TNG model assumes  $A_{\text{SN1}} = 3.6$ . The DREAMS simulations vary over  $A_{\text{SN1}}$  in logarithmic space from 0.9 to 14.4.<sup>3</sup>

The speed of stellar winds is defined such that

$$v_w = \max \left[ A_{\text{SN2}} \sigma_{\text{DM}} \left( \frac{H_0}{H(z)} \right)^{1/3} , v_{w, \text{min}} \right] , \quad (4)$$

where  $A_{\text{SN2}}$  is a dimensionless normalization factor,  $H(z)$  is the Hubble parameter at redshift  $z$ ,  $v_{w, \text{min}}$  is the minimum wind speed (set to  $350 \text{ km s}^{-1}$ ), and  $\sigma_{\text{DM}}$  is the velocity dispersion of the 64 nearest dark matter particles. The fiducial value of  $A_{\text{SN2}}$  in TNG is 7.4; in DREAMS, it is varied logarithmically from 3.7 to 14.8.

<sup>3</sup> The parameter variations are performed in log space for  $A_{\text{SN1}}$ ,  $A_{\text{SN2}}$ , and  $A_{\text{AGN}}$  because these are all multiplicative factors. Varying them in log space ensures that the sampling is symmetric in terms of fractional changes rather than absolute values. In practice, this is especially useful since these amplitudes can span several orders of magnitude: a log scaling guarantees that, e.g., doubling and halving a parameter are treated as equally significant variations.

The imposed floor on the wind speed can potentially diminish the impact of varying  $A_{\text{SN}2}$ , particularly in low-mass satellites and at high redshifts. Indeed, the wind speed floor in the fiducial TNG model increases the efficacy of feedback at early times (Pillepich et al. 2018a).

Note that  $A_{\text{SN}1}$  and  $A_{\text{SN}2}$  enter in the mass-loading factor of Equation 2 differently. The energy injection rate can be quantified via

$$\dot{E}_{\text{wind}} \propto \eta v_w^2. \quad (5)$$

The impact of  $A_{\text{SN}1}$  is clear: increasing  $A_{\text{SN}1}$  raises the mass-loading factor, which increases the energy injection rate. Increases to  $A_{\text{SN}2}$ , on the other hand, have a more subtle effect. By increasing  $A_{\text{SN}2}$ , the wind speed increases, however, the mass-loading factor is proportionally decreased (since  $\eta \propto v_w^{-2}$ ) keeping the energy injection rate fixed. It then is a question of whether launching less material faster has a stronger impact on the system than more material slower. Here we define “efficacy” in terms of the galaxy-scale consequences of feedback, such as reduced stellar mass growth and stronger baryon removal, instead of in terms of the instantaneous energy injection rate (which is fixed in the case of  $A_{\text{SN}2}$  variations). We find that, for the range of values probed in this work, increasing  $A_{\text{SN}2}$  increases the “efficacy”—by our definition—of feedback-driven winds (i.e., in this part of the TNG model parameter space it is more effective to drive slightly less material at slightly faster speeds). We show this effect explicitly in Section 3.3.

Feedback from AGN in the TNG model is implemented in one of two channels based on the accretion rate of the central supermassive black hole (see Weinberger et al. 2018, for a complete description of the AGN and black hole model in TNG). Low accretion rates correspond to a ‘kinetic mode’ of feedback where winds are driven in a pulsed and directed fashion, whereas high accretion rates describe a ‘thermal mode’ of feedback where thermal energy is continuously dumped into the surroundings. The thermal mode of feedback dominates for TNG galaxies with stellar masses  $\lesssim 10^{10.5} M_\odot$ , while galaxies with larger stellar masses are dominated by kinetic-mode feedback (Weinberger et al. 2017). Since the Milky Way hosts in DREAMS spend most—if not all—of their lives below this stellar mass, only the thermal feedback mode is varied in this suite. Specifically, the normalization of the continuous thermal-feedback energy is varied, given by

$$\dot{E}_{\text{AGN}} = \epsilon_r A_{\text{AGN}} \dot{M}_{\text{BH}} c^2, \quad (6)$$

where  $\epsilon_r$  is the radiative efficiency,  $A_{\text{AGN}}$  is the fraction of energy that is transferred to the nearby gas, and  $\dot{M}_{\text{BH}}$  is the accretion rate onto the black hole. The fiducial

$A_{\text{AGN}}$  parameter is 0.1 in TNG and is varied logarithmically from 0.025 to 0.4 in DREAMS.

The original suite of TNG simulations was run using Planck Collaboration et al. (2016) cosmology (Pillepich et al. 2018a). DREAMS varies the cosmology according to the 16<sup>th</sup> and 84<sup>th</sup> bounds on the values of  $\Omega_M$  and  $\sigma_8$  from Planck Collaboration et al. (2014, see their Table 2) multiplied by a factor of two as a proxy for a two-standard-deviation uncertainty. The two cosmological parameter variations are sampled linearly in DREAMS.

## 2.2. Reconstruction of Dark Matter Density

The simulation dark matter is modeled as a collection of (large) discrete particles in TNG (see Section 2.1 for mass resolution). Since the goal of this paper is to study the dark matter profiles, we need to “reconstruct” a continuous density from these discrete particles. To obtain the density at each point in space, we distribute the mass of a single dark matter particle according to a smooth particle hydrodynamics kernel weighting scheme (e.g., Monaghan 1992; Springel 2010b). The density at a location in space,  $s$ , is computed as

$$\rho_s = \sum_n^{N_{\text{ngb}}} m_n W(r_n | h_{\text{sml}}), \quad (7)$$

where  $m_n$  is the mass of the  $n^{\text{th}}$  neighboring particle,  $W$  is the kernel weighting function (with units of inverse volume),  $N_{\text{ngb}}$  is the number of nearest neighbors,  $r_n$  is the distance between the point  $s$  to the  $n^{\text{th}}$  particle, and  $h_{\text{sml}}$  is the smoothing length of the kernel. The adopted kernel is a top hat, which takes the form

$$W(r | h_{\text{sml}}) = \begin{cases} \frac{3}{4\pi h_{\text{sml}}^3} & |r/h_{\text{sml}}| \leq 1 \\ 0 & \text{otherwise} \end{cases}. \quad (8)$$

The smoothing length is determined by finding the maximum distance to the nearest 32 neighbors using SCIPY.SPATIAL.KDTREE (Virtanen et al. 2020). It should be noted that the top-hat kernel estimates slightly higher densities (by  $\sim 5\%$ ) than other common kernel density functions (cubic spline or Gaussian) due to its shape (see, e.g., Qi et al. 2025, their Appendix A); however, this change does not systematically change any of the core results of this work.

We sample radially in 300 bins ranging from 2.8 times the softening length ( $\sim 1.2$  kpc) to 600 kpc.<sup>4</sup> At each

<sup>4</sup> For distances greater than  $\sim 2.8\times$  the softening length, gravity is fully Newtonian, whereas below this scale the shape of the potential is impacted significantly by the choice of softening length (Ludlow et al. 2020). We therefore omit any radial bins at  $< 1.2$  kpc from the center of the halo.



radius, we sample this reconstructed density field uniformly along a spherical shell with  $10^3$  points. We take the average density on this shell as the density at that particular radial location. We also calculate a standard deviation of densities at each radial bin as a measure of azimuthal variations of the density within our shell. We find that the typical standard deviation of densities is  $\lesssim 0.1$  dex at all radii within  $R_{200}$ , suggesting that the halos are reasonably spherical—even while include the contribution from satellites. We leave a more careful examination of the three-dimensional shape of the dark matter halos for a future work.

### 2.2.1. Fitting Analytic Profiles

In Section 3.2.2, we fit each profile with an analytic function to get a more quantitative understanding of the shape of the dark matter density profiles. We fit the profiles with a generalized NFW (gNFW) profile of the form

$$\rho(r) = \frac{\rho_s}{\left(\frac{r}{r_s}\right)^\gamma \left[1 + \left(\frac{r}{r_s}\right)^\alpha\right]^{(\beta-\gamma)/\alpha}}, \quad (9)$$

where  $\rho_s$  and  $r_s$  are the scale density and radius (respectively),  $\gamma$  is the inner slope,  $\beta$  is the outer slope, and  $\alpha$  regulates how sharply the transition between the two occurs (e.g., Jaffe 1983; Hernquist 1990; Zhao 1996; Merritt et al. 2006; Di Cintio et al. 2014). In the case that  $\alpha = 1$ ,  $\beta = 3$ , and  $\gamma = 1$  the gNFW profile is identical to that of the canonical NFW profile (i.e., Equation 1).

We fit the gNFW profiles using an iterative procedure to obtain priors for the free parameters and ensure convergence. First, we fit a standard NFW profile to obtain priors on  $\rho_s$  and  $r_s$  using non-linear least squares minimization (SCIPY.OPTIMIZE.CURVEFIT; Virtanen et al. 2020). We then fit a gNFW profile with  $\rho_s$  and  $r_s$  fixed to the NFW values to derive priors for the shape parameters ( $\alpha, \beta, \gamma$ ; again using non-linear least-squares minimization). Finally, we perform a full Markov Chain Monte Carlo (MCMC) fit using the EMCEE package (Foreman-Mackey et al. 2013), allowing all five parameters to vary simultaneously. The MCMC fitting uses a Gaussian likelihood of the form

$$\log L(\theta) = -\frac{1}{2} \sum \left( \frac{\log \rho - \log \rho_{\text{model}}(r|\theta)}{\sigma_\rho} \right)^2, \quad (10)$$

where  $\log \rho$  is the measured average density profile in each radial bin,  $\log \rho_{\text{model}}(r|\theta)$  is the gNFW prediction at radius  $r$  given fit parameters  $\theta$ , and  $\sigma_\rho$  is the standard deviation of densities about the average profile. We adopt broad Gaussian priors centered on the values obtained from the previous steps using a factor of  $5\times$  the uncertainty on the non-linear least squares fits (given by

square root of covariance matrix along the diagonal) as the width of the Gaussian prior. This ensures the gNFW fits are not restricted to NFW-like solutions but instead use the NFW fit only to guide initialization. Finally, we note that we limit this fitting procedure to radii less than  $R_{200}$ .

### 2.3. Emulators

Throughout this work, we employ a neural network emulator to act as a multi-dimensional interpolator of the parameter space sampled in the DREAMS simulations. These emulators are trained to predict summary statistics of the simulations as a function of the underlying cosmological and astrophysical parameters. By learning the complex, non-linear mappings between input parameters and simulated outputs, the emulator efficiently explores parameter dependencies and makes predictions without the computational cost of running additional simulations. The emulator also provides estimates of prediction uncertainty, enabling robust marginalization over multiple parameters at once. We briefly describe our emulator in this section, noting that is very similar in both spirit and implementation to that of Rose et al. (2025).

Our emulators take the five simulation parameters as input:  $A_{\text{SN1}}$ ,  $A_{\text{SN2}}$ ,  $A_{\text{AGN}}$ ,  $\Omega_{\text{M}}$ , and  $\sigma_8$ . These inputs are fed into a series of fully connected layers which output a prediction for the mean and standard deviation of the quantity of interest. The loss function is defined as

$$\mathcal{L} = \sum_{\text{batch}} (\theta - \mu)^2 + \sum_{\text{batch}} [(\theta - \mu)^2 - \sigma^2]^2, \quad (11)$$

where  $\theta$  is the true value of the target in each simulation,  $\mu$  is the predicted mean, and  $\sigma$  is the predicted standard deviation. This loss function minimizes the mean-squared-error of the data (first term) while also ensuring that the measured deviation is reproduced (second term). It allows the network to learn both accurate predictions and well-calibrated uncertainties (Jefrey & Wandelt 2020; Villaescusa-Navarro et al. 2022; Rose et al. 2025).

We split the data into training, validation, and test sets, which comprise 80%, 10%, and 10% of the dataset, respectively. We optimize our models using the OPTUNA package (Akiba et al. 2019) to select: (i) the number of fully connected layers, (ii) the nodes in each layer, (iii) the learning rate, (iv) the weight decay, and (v) the dropout rate. Following directly from Rose et al. (2025), we vary the number of layers from 1 to 5, the number of neurons from 4 to  $10^3$ , the learning rate from  $10^{-5}$  to  $10^{-1}$ , the weight decay from  $10^{-8}$  to 1, and the dropout rate from 0.2 to 0.8. The hyperparameter tuning is done using 50 trials consisting of 500 epochs each.

We employ emulators in six places in this work to output gNFW shape parameters (Figures 3 and 4 in Section 3.2), dark matter mass growth in the inner regions of halos (Figure 5 in Section 3.3), the stellar mass and black hole mass of the central galaxies (Figure 6 in Section 3.3), the lifetime feedback energy output by AGN (Figure 10 in Appendix A), and fitting parameters for our adiabatic contraction calculations (Figure 12 in Appendix C). In each case, we hyperparameter optimize and train ten instances of the emulator with different random initializations of the weights (for a total of 50 models created for this work). In all the results showing predictions from the emulators, we report the mean of the predictions from the ten instances. Each instance we report in this work is comprised of emulation of 1000 halos of a single parameter variations keeping the other parameters fixed at their fiducial TNG values. This means that, e.g., for each panel in Figure 3 there are a total of  $10 \times 1000$  draws from the emulators (for a total of 50,000 in the whole figure). For the uncertainty on the predictions we quote

$$\sigma_{\text{total}}^2 = \bar{\sigma}_{\text{pred}}^2 + \sigma_{\text{ensemble}}^2 \quad (12)$$

where  $\bar{\sigma}_{\text{pred}}$  is the average predicted uncertainty from each initialization of the emulator, which serves as a proxy for the halo-to-halo variance, and  $\sigma_{\text{ensemble}}$  is the epistemic uncertainty, which captures the uncertainty of the network itself. Regardless, we find that the epistemic uncertainty is always negligible compared to the halo-to-halo variation.

We show an example validation of our emulator to predict the gNFW shape parameters in Figure 14 (Appendix D).

#### 2.4. Halo Weighting Scheme

The TNG model has undoubtedly proven to be a widely successful and useful tool for understanding galaxy evolution, yet, as we show in this work, it is not completely robust to the changes in feedback and cosmology of DREAMS. Put simply, not all of the halos reproduce realistic systems due to our feedback variations. We therefore report all of the main summary statistics (see left panels of Figures 2, 7, and 8) with weights that reflect whether the halos are consistent with observed galaxies, rather than assuming all halos contribute equally. All quantities that are weighted will be denoted with the overhead “hat” (e.g.,  $\hat{\sigma}$ ).

To quantify how realistic a galaxy’s properties are, we follow the weighting criteria outlined in [Rose et al. \(In Prep; Centrals\)](#). That work “scores” a simulation based on the halo/galaxy’s properties and how they compare to well-established scaling relations from observations.

The three scaling relations used in that work are the stellar mass-halo mass relation ([Wang et al. 2024](#)), mass-metallicity relation ([Curti et al. 2020](#)), and black hole mass-velocity dispersion relation ([Greene et al. 2020](#)). A system’s score is based on the distance to the relation and is normalized to the scatter about the relation such that

$$\delta_{i,j} = \frac{(\phi_{i,j} - \mu_j)^2}{\sigma_j^2}, \quad (13)$$

where  $\phi_{i,j}$  is the property of the system in the  $i^{\text{th}}$  simulation for the  $j^{\text{th}}$  scaling relation,  $\mu_j$  is the observed value on the scaling relation, and  $\sigma_j$  is the scatter about the relation. The weights for each scaling relation are then calculated using

$$W_i = e^{-\delta_{i,j}/2}, \quad (14)$$

with a galaxy’s total weight being the product of the individual weights for each scaling relation. Rather than calculating a weight for each individual system that may be sensitive to the detailed accretion and/or formation history of the halo, we bin parameter space and calculate weights based on the average properties in each bin. The results of this weighting procedure can be seen in Figure 2 of [Rose et al. \(In Prep; Centrals\)](#). To briefly summarize, we find that these three scaling relations down-weight the extreme values of  $A_{\text{SN1}}$  and  $A_{\text{SN2}}$  and the lower-than-fiducial values of  $A_{\text{AGN}}$ , but do not place strong constraints on  $\Omega_{\text{M}}$  or  $\sigma_8$ .

We note that our main conclusions are not particularly sensitive to using this weighting scheme. However, since there are galaxies in our sample that are unrealistic, we aim to down weight their contributions.

### 3. RESULTS

#### 3.1. Dark Matter Density Profiles

Figure 2 shows the dark matter density profiles for all of the DREAMS halos (large panel on left). To compare the results across simulations, the radii are normalized by  $R_{200}$  for each galaxy. Moreover, we include our weighting scheme for the distribution of density profiles in the left-hand panel. The mean and standard deviation therefore indicate the variation of density profiles for those Milky Way halos whose central galaxies are more consistent with observations.

On the whole, the dark matter profiles are largely consistent in terms of normalization, which is, in part, by construction of the selection function of the DREAMS halos. There is a tight (weighted) spread in densities of 0.13 dex at  $0.1R_{200}$  ( $\sim 20$  kpc). At larger radii, the spread increases by a factor of  $\sim 2$  (0.28 dex at  $R_{200}$ ) which is a feature of the halos containing many



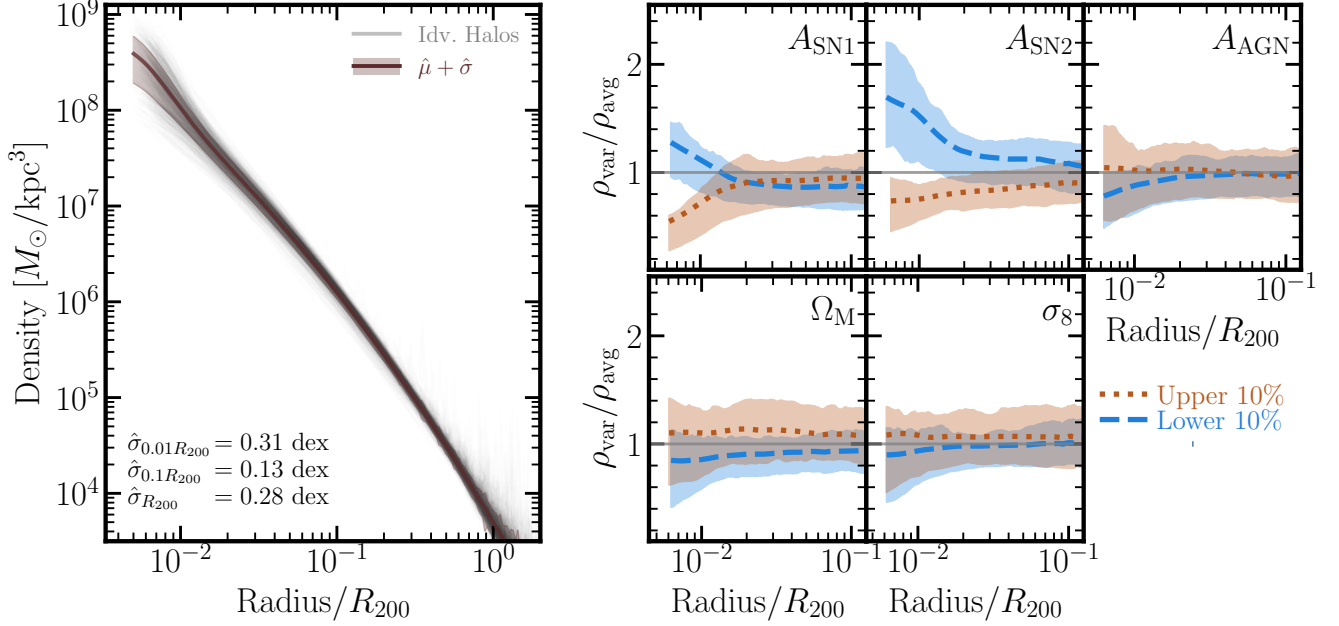


**Figure 2. Dark Matter Density Profiles in the DREAMS CDM Milky Way-Mass Suite.** The large left-hand panel shows the dark matter density as a function of radius for all halos in the DREAMS CDM Milky Way-mass suite from  $\sim 1.2$  kpc to 600 kpc (normalized by  $R_{200}$ ). The red line and shaded regions correspond to the weighted mean and standard deviations of the individual profiles (see Section 2.4 and [Rose et al. \(In Prep; Centrals\)](#) for details on the weighting procedure). The values in the bottom left of the large panel correspond to the weighted standard deviation of densities at  $0.01R_{200}$  ( $\sim 2$  kpc),  $0.1R_{200}$  ( $\sim 20$  kpc), and  $R_{200}$  ( $\sim 200$  kpc). The panels on the right break down the upper and lower 10% of the distribution of densities according to variations in  $A_{\text{SN1}}$  (top left),  $A_{\text{SN2}}$  (top middle),  $A_{\text{AGN}}$  (top right),  $\Omega_{\text{M}}$  (bottom left), and  $\sigma_8$  (bottom middle) for the inner 12 kpc. The colored line in each of the panels is the median density profile for the upper (dotted orange) and lower (dashed blue) 10% of the parameter while the colored shaded region represents the 25<sup>th</sup> and 75<sup>th</sup> percentile (inner quartile range) of profiles within the parameter range. Overall, the profiles are very much self-similar, with a modest amount of scatter. Moreover, the baryonic parameters primarily affect the central densities.

subhalos at these large radii. The presence of more satellites leads to occasional “spikes” to higher densities at large radii. In the inner-most regions of the halo,  $0.01R_{200}$  ( $\sim 2$  kpc), there is a much wider distribution of densities with a spread of 0.31 dex (a factor of  $\sim 2.5$  increase from  $0.1R_{200}$ ).

The variation in the inner regions of the halo is primarily driven by the variations in the supernova physics. To show this concretely, each panel on the right of Figure 2 shows the profiles broken down into the upper and lower 10% of the simulation parameter distributions. These percentiles represent  $\sim 100$  halos each that have the highest (or lowest) values of each individual parameter while marginalizing over all the others. The lines in the small panels of Figure 2 represent the median profile of halos within each percentile (dotted from upper 10% and dashed for lower 10%) while the shaded region shows the inner quartile range (25<sup>th</sup> and 75<sup>th</sup> percentiles) of profiles in each bin. The top row shows the astrophysical parameter variations:  $A_{\text{SN1}}$  in top left,  $A_{\text{SN2}}$  in top middle, and  $A_{\text{AGN}}$  in the top right. The bottom row shows

	Upper 10%	Lower 10%	Consistent with 1?
$A_{\text{SN1}}$	$0.546^{+0.059}_{-0.268}$	$1.278^{+0.185}_{-0.315}$	No and Yes
$A_{\text{SN2}}$	$0.737^{+0.213}_{-0.281}$	$1.697^{+0.508}_{-0.463}$	No
$A_{\text{AGN}}$	$1.045^{+0.387}_{-0.486}$	$0.782^{+0.207}_{-0.295}$	Yes and No
$\Omega_{\text{M}}$	$1.101^{+0.321}_{-0.481}$	$0.848^{+0.279}_{-0.432}$	Yes
$\sigma_8$	$1.082^{+0.263}_{-0.529}$	$0.899^{+0.250}_{-0.436}$	Yes

**Table 2. Ratio of Densities Relative to the Average Profile.** The median ratio of the parameter variation density profiles ( $\rho_{\text{var}}$ ) to average profile ( $\rho_{\text{avg}}$ ) for each DREAMS simulation parameter’s upper and lower 10% ranges (shown in the right-hand panels of Figure 2). The values shown here are taken at the inner most radius we probe ( $0.006R_{\text{vir}}$ ). The scatter here corresponds to the 25<sup>th</sup> and 75<sup>th</sup> percentiles of the distributions.

the cosmological parameter variations:  $\Omega_{\text{M}}$  in the bottom left and  $\sigma_8$  in the bottom middle.

We report we report the density ratios at  $0.006R_{200}$  when varying different baryonic parameters in Table 2 taken at the inner most radii we probe ( $\sim 0.006R_{200}$ ,

or an average of  $\sim 1.5$  kpc). We caution that this metric does not guarantee that deviations from the average profiles are specifically caused by the variations (or lack thereof) in the simulation parameter. Since these are the raw simulation outputs, deviations could also be driven by the combination of co-variation of the supernovae parameters and halo-to-halo variance. To that end, we probe the one-parameter dependencies more directly in the following section using our neural network emulator.

We find that the lower  $A_{\text{SN1}}$  values correspond to a median density ratio of  $1.278^{+0.185}_{-0.315}$ , while the higher  $A_{\text{SN1}}$  values have a median ratio of  $0.737^{+0.213}_{-0.281}$ . This represents an average factor of  $\sim 30\%$  increase in the central density, while higher values reduce these densities by  $\sim 30\%$ . However, within the halo-to-halo variance the lower  $A_{\text{SN1}}$  variations are consistent with no significant change. For  $A_{\text{SN2}}$ , the lower values correspond to a ratio of 1.697 (spread of  $+0.508$  and  $-0.463$ ) and the higher values correspond to a ratio of 0.737 (spread of  $+0.213$  and  $-0.281$ ). This is an average  $\sim 60\%$  enhancement in densities for low  $A_{\text{SN2}}$  values and a  $\sim 40\%$  decrease for high  $A_{\text{SN2}}$ . Notably, neither the upper or lower  $A_{\text{SN2}}$  parameter variations are consistent with the average profile. Interestingly, the enhancement/decrease caused by  $A_{\text{SN2}}$  (which controls wind speed in our simulations) extends to much larger radii than those of  $A_{\text{SN1}}$  (which controls wind energy).

In terms of  $A_{\text{AGN}}$ , the upper values are consistent with the average profile (ratio of  $1.045^{+0.387}_{-0.486}$ ), while the lower values are very slightly lower than the average profile (ratio of  $0.782^{+0.207}_{-0.295}$ ). While very slight, this decrease in central density with decreased  $A_{\text{AGN}}$  is likely related to a self-regulation of the black holes which we discuss in more detail in Section 3.3. For both the  $\Omega_{\text{M}}$  and  $\sigma_8$  variations, on the other hand, both the lower and upper variations of these parameters are consistent with the average profile.

### 3.2. Analytic Fits to Profiles

#### 3.2.1. Scale Density

We now examine how the best-fit gNFW parameters change as a function of the DREAMS astrophysics and cosmology variations (see Section 2.2.1 for fitting procedure). Figure 3 shows the scale density  $\rho_s$  as a function of the five parameters. More specifically, we show the predictions made by an emulator trained to learn the one-parameter dependence of  $\rho_s$  (see Section 2.3 for details on the training and hyperparameter optimization). The advantage of this approach, compared to showing all the fits to the profiles in Figure 2, is that we are able to directly parameterize the dependence of  $\rho_s$  on a parameter-by-parameter basis, instead of sampling

from realizations that have multi-parameter dependencies. We therefore keep the other four fixed to their fiducial TNG value for each individual simulation parameter variation. The solid lines are the average predictions of the ensemble of ten emulators which have different initial weighting realizations. Each shaded region represents the  $1\sigma$  uncertainty of the ensemble of emulators via Equation 12, which gives a proxy for the intrinsic halo-to-halo scatter at a given parameter point. Finally, we note that the vertical solid red line at the top of each panel marks the fiducial TNG parameter (from Table 1).

We find that the average  $\rho_s$  has some dependency on all five of the simulation parameters over the parameter limits explored in this work, albeit (i) to different extents and (ii) at the few percent level. The parameter that seems to hold the most importance in setting the scale density is  $A_{\text{SN2}}$  (top middle panel of Figure 3). In fact,  $\log \rho_s$  seems to be roughly inversely proportional to  $\log A_{\text{SN2}}$  – ranging from values of  $\rho_s = 10^{7.1} \text{ M}_{\odot} \text{ kpc}^{-3}$  at the lowest  $A_{\text{SN2}}$  values to  $\rho_s = 10^{6.8} \text{ M}_{\odot} \text{ kpc}^{-3}$  at the highest values of  $A_{\text{SN2}}$ , a change of  $\sim 0.3$  dex. In comparison, the average halo-to-halo variance for  $A_{\text{SN2}}$  is 0.206 dex (shaded region in each panel). Thus, the impact of  $A_{\text{SN2}}$  is more significant than the intrinsic scatter of the sample, but only by 0.1 dex. For the other supernova parameter,  $A_{\text{SN1}}$ ,  $\rho_s$  seems to have no dependence at less-than-fiducial values, but has a trend of decreasing  $\log(\rho_s)$  with increasing  $\log(A_{\text{SN1}})$  (top left panel) at higher values. The mean scale density changes by 0.2 dex from the fiducial TNG value to the highest  $A_{\text{SN1}}$  we probe in this work; however, the average halo-to-halo scatter is 0.22 dex for  $A_{\text{SN1}}$ . We therefore conclude that there is not a very strong trend with the supernova wind energy ( $A_{\text{SN1}}$ ), despite there being a stronger trend with the supernova wind speed ( $A_{\text{SN2}}$ ).

Similar to  $A_{\text{SN1}}$ , the scale density seems to have very little dependence on any of the other simulation parameters. The total variation in the mean relation for  $A_{\text{AGN}}$  is  $\sim 0.2$  dex, for  $\Omega_{\text{M}}$  it is  $\sim 0.1$  dex, and for  $\sigma_8$  it is  $\sim 0.15$  dex. All of these are less than their respective halo-to-halo scatters of 0.21 dex.

Despite not being significantly larger than halo-to-halo variation, it is interesting to note that at values greater than the fiducial  $A_{\text{AGN}}$ , the scale density seems to *increase* with increasing AGN feedback strength. This increase in density with increasing AGN feedback is consistent with the results from the previous section. We, again, suspect that the AGN variations is due to a self-regulation of black hole masses at high feedback: at a certain point the feedback prevents the black holes from growing, leading to a lack of additional feedback

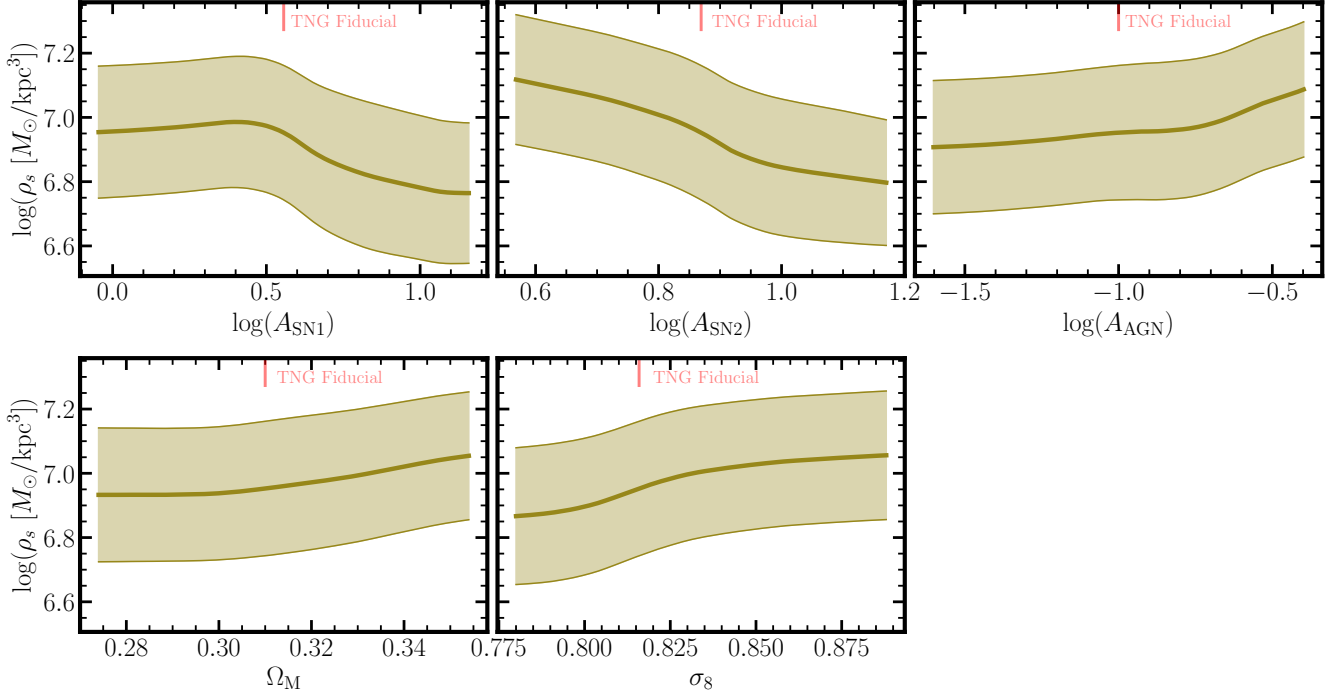


**Figure 3. Dependence of generalized NFW scale density ( $\rho_s$ ) on Astrophysics and Cosmology.** Predictions from an ensemble of emulators (see Section 2.3) for the scale density,  $\rho_s$ , of the DREAMS CDM Milky Way-mass density profiles. We show the predictions made by the emulator as a function of  $A_{\text{SN1}}$  (top left),  $A_{\text{SN2}}$  (top middle),  $A_{\text{AGN}}$  (top right),  $\Omega_M$  (bottom left), and  $\sigma_8$  (bottom middle). The shaded regions represent the one standard deviation uncertainty of the predictions based on the individual model prediction uncertainty as well as variance across the emulators (via Equation 12). The vertical red solid line at the top of each panel corresponds to the fiducial TNG value (see Table 1). While not shown, the emulator also predicts the scale radius. We find that the trends for the scale radius are identical to those shown here, just in the opposite direction (i.e., increasing  $A_{\text{SN2}}$  increases  $r_s$ ).

energy from the black hole (we explore this argument in more detail in both Section 3.3 and Appendix A).

In summary, we find that the halo-to-halo variation is the dominant driver of the normalization of the dark matter density profiles. With the exception of supernova wind speed ( $A_{\text{SN2}}$ ), none of the DREAMS simulation parameters drive variations more significant than the halo-to-halo variations. While not shown, we obtain qualitatively similar trends for the scale radius  $r_s$  (in the opposite direction as  $r_s$  and  $\rho_s$  are inversely proportional to each other).

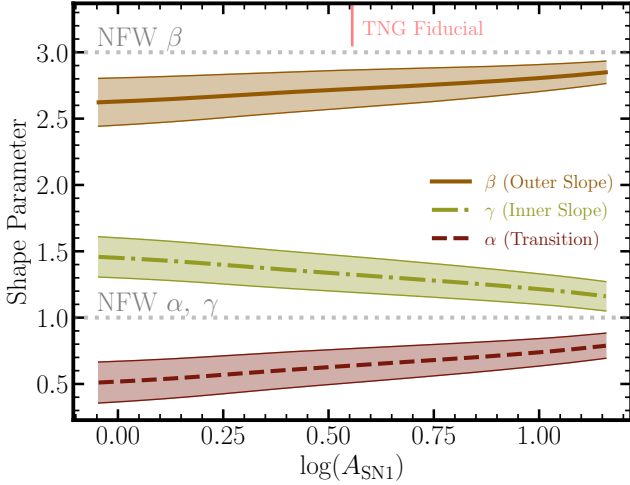
### 3.2.2. Profile Shape Parameters

Figure 4 shows the best-fit shape parameters  $\beta$  (outer slope),  $\gamma$  (inner slope) and  $\alpha$  (transition rate) for the gNFW profile as a function of  $A_{\text{SN1}}$ . We note that, within the uncertainty of halo-to-halo scatter, the shape parameters do not depend sensitively to any other parameter. The dotted gray line on Figure 4 represents values of  $\alpha = \gamma = 1$  which are consistent with a canonical NFW profile.

We find that with increasing  $A_{\text{SN1}}$  all the shape parameters tend towards the values for the canonical NFW

profile. Importantly, the NFW profile is the empirical prediction from DMO simulations (Navarro, Frenk, & White 1997). What is happening here is that these extremely high wind energy variations of the TNG model prevent the growth of any significant stellar component (which we show explicitly in Section 3.3), thus the halos are less dominated by the presence of baryons and behave more like collisionless DMO simulations. It should be noted, though, that the gNFW shape parameters only tend towards the NFW values and do not actually reach them in the  $A_{\text{SN1}}$  variations we make here. Thus, while the stronger feedback is preventing the growth of the stellar mass, it is not entirely prevented leading to a density profile that is *almost* that of an NFW profile (but notably not exactly an NFW). We explore the stellar mass growth (or lack thereof) further in the next section and in Rose et al. 2025 (In Prep; both).

It is interesting to note that the variations to the supernova wind *energy* ( $A_{\text{SN1}}$ ) seem to drive the shape of the dark matter density profiles, while changes to the supernova wind *speed* ( $A_{\text{SN2}}$ ) has a stronger impact on the normalization of the profile. It is possible that ejecting winds faster (as is the case with  $A_{\text{SN2}}$ ) can more effi-



**Figure 4. Dependence of generalized NFW shape parameters on  $A_{\text{SN1}}$ .** Predictions from our neural network emulator for the dependence of the inner slope ( $\gamma$ ; dot dashed line), transition rate ( $\alpha$ ; dashed line), and outer slope ( $\beta$ ) of the best-fit gNFW profiles on the supernova wind energy ( $A_{\text{SN1}}$ ). As a point of reference, the dotted gray lines show the canonical NFW profile values ( $\alpha = \gamma = 1$  and  $\beta = 3$ ). The short vertical solid line at the top corresponds to the fiducial TNG value of  $A_{\text{SN1}} = 3.6$  (see Table 1; Section 2.1.1). The average prediction lines are the mean of our ten emulators while the shaded regions approximate the halo-to-halo variation (although there is also a small contribution from the combination of emulators, see Section 2.3 for details). We note that, within the uncertainty due to halo-to-halo variation the shape parameters have no dependence on any of the other DREAMS simulation parameters.

ciently disrupt the potential, changing the dark matter density, compared to increases to the total feedback energy ( $A_{\text{SN1}}$ ) which is better at suppressing the growth entirely of the baryon component of the galaxy.

Overall, we find that the single most important feature in setting the normalization and shape of density profiles for Milky Way-mass halos in the TNG model is halo-to-halo variance. Beyond halo-to-halo scatter, extreme variations to supernova feedback can slightly change the overall normalization ( $A_{\text{SN2}}$ ) or its shape ( $A_{\text{SN1}}$ ) beyond that of the intrinsic scatter.

### 3.3. Central Dark Matter Mass Growth

In the previous section, we quantified the relative role that baryon feedback, cosmology, and intrinsic halo-to-halo variation play on the overall shape and normalization of the DREAMS dark matter halos. Here, we further assess the relative contribution of these three features by using the “central mass growth” of the halos,

$$\Gamma_{0.01} = \log \left[ \frac{M_{\text{enc, Hydro}}(0.01R_{200})}{M_{\text{enc, DMO}}(0.01R_{200})} \right], \quad (15)$$

defined as the logarithmic ratio of dark matter mass enclosed at  $0.01R_{200}$  from hydro-to-DMO (similar to the metric used in Rose et al. 2023). This quantity provides a metric for the changes in the inner dark matter distribution relative to a DMO baseline. Dark matter will contract because of the presence of the baryons (see also discussion in Section 4.2, and thus this  $\Gamma_{0.01}$  should also be sensitive to the detailed behavior set by the feedback variations.

Figure 5 shows the central mass growth as a function of the three DREAMS baryonic feedback parameters (we find no systematic trend with cosmology variations). As in Section 3.2, we train an ensemble of emulators to learn the single parameter dependency of the central mass growth (see Section 2.3 for more details on the emulator training process) and report the average predictions (solid line) and halo-to-halo variation (shaded region). We find that all of the three astrophysics parameters have significant impacts on the central mass growth of the halos. The average halo-to-halo variation is 0.12 dex for each variation, whereas we find variations of  $\sim 0.5$  dex,  $\sim 0.4$  dex, and  $\sim 0.2$  dex for  $A_{\text{SN1}}$ ,  $A_{\text{SN2}}$ , and  $A_{\text{AGN}}$ , respectively.

The lowest  $A_{\text{SN1}}$  values cause a central mass increase of  $\sim 0.55$  dex (a factor of  $> 3$ ) while the highest  $A_{\text{SN1}}$  values only increase the central mass by  $\sim 0.05$  dex. The decrease in mass growth from the lowest-to-highest  $A_{\text{SN1}}$  values is not linear, however. Around the fiducial TNG value ( $\log A_{\text{SN1}} = 0.55$ ), the central mass growth decreases more rapidly with increasing  $\log A_{\text{SN1}}$  until  $\log A_{\text{SN1}} \sim 0.7$ . The  $A_{\text{SN2}}$  variations yield a very similar trend to that of  $A_{\text{SN1}}$ , albeit with a less sharp decrease at high values. Both the  $A_{\text{SN1}}$  and  $A_{\text{SN2}}$  trends follow trends seen in the stellar mass of the central galaxy, as demonstrated in the left two panels of Figure 6. In the low  $A_{\text{SN1}}$  and  $A_{\text{SN2}}$  regime, the feedback may no longer be strong enough to prevent gas from further collapsing, thus all the baryons that would have turned into stars eventually do. Interestingly, it appears that the saturation limit for feedback regulating further star formation is just less than the fiducial TNG values of  $A_{\text{SN1}}$  and  $A_{\text{SN2}}$ , potentially owing to the fixed star formation efficiency in the TNG model. At the other end, the strong supernova feedback likely disrupts gas that would have otherwise formed stars and removes it from the system entirely. The net effect of several of these disruptions over the lifetime of the system leads to an overall decrease in the overall stellar mass of the galaxy. Regardless of the exact physical mechanism, it is clear that the conclusion from previous sections holds here as well: stronger feedback ( $A_{\text{SN1}}$  in particular) prevents



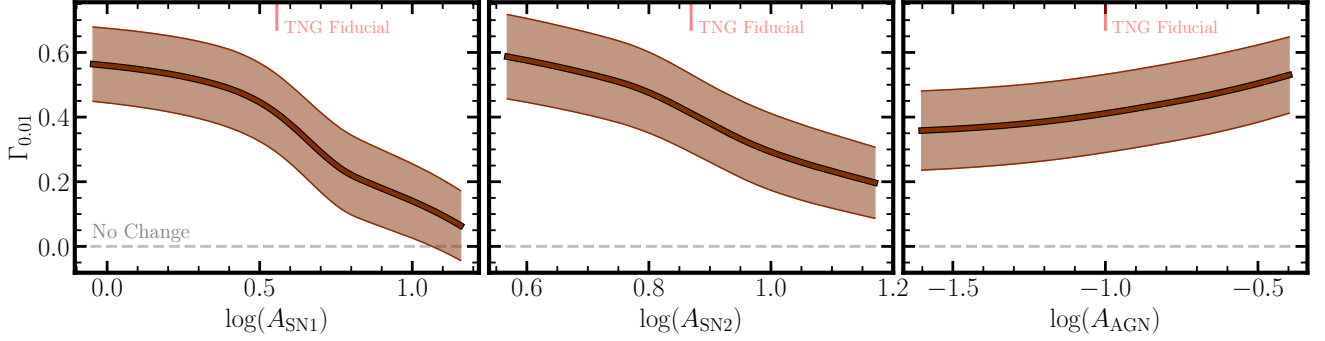


**Figure 5. Central Mass Growth ( $\Gamma$ ) of Halos at  $0.01R_{200}$ .** Predictions from our emulators for the central mass growth, defined as the ratio of the dark matter mass in the hydro simulations to that of the DMO simulations (see Equation 15), as a function of the three DREAMS baryon feedback parameters. The solid line represents the average prediction of the parameter from the ensemble of emulators, while the shaded region is the uncertainty on the predictions as a proxy for halo-to-halo variance (via Equation 12). The dashed gray line represents a mass ratio of unity, where the halo mass is unchanged from the hydro to the DMO simulation. The short solid lines at the top of each panel correspond to the fiducial TNG value (see Table 1). We find that the supernova feedback parameters decrease the central mass, whereas the AGN feedback parameter increases the central mass.

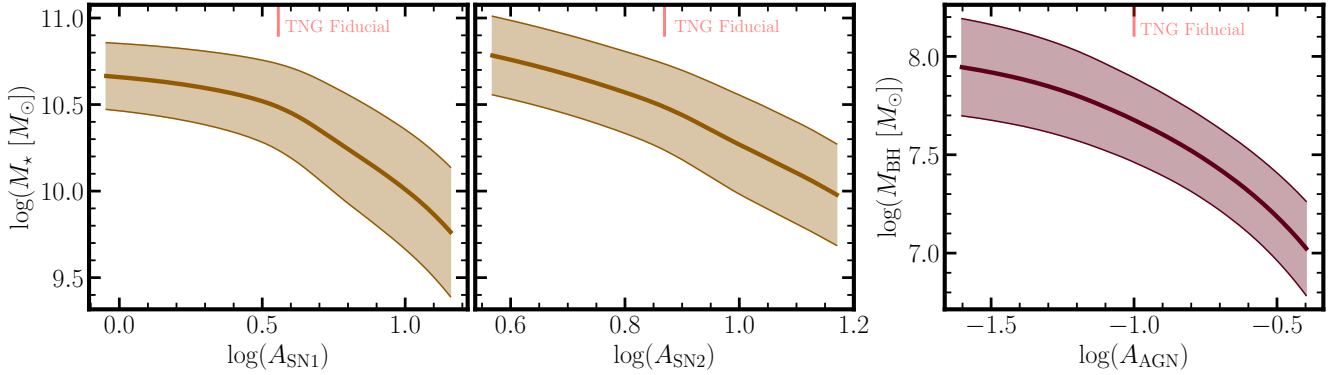


**Figure 6. Properties of Central Galaxy.** Predictions from our emulator for the scaling of the stellar mass (left two panels) and black hole mass (right panel) of the Milky Way-mass halo's central galaxy with the DREAMS astrophysics variations. The solid line represents the aggregate predictions from ten emulators while the shaded region is the uncertainty on the models (same as, e.g., Figure 5). Increased supernova feedback (both wind energy and speed) decreases the stellar mass of the central galaxy, while increased AGN feedback actually *decreases* the central supermassive black hole.

baryon formation sufficiently easily that the simulations are nearly DMO.

The AGN variations follow a different trend, on the other hand. With increasing  $\log A_{\text{AGN}}$ , there is a roughly linear increase in the central mass growth; ranging from  $\sim 0.35$  dex to  $\sim 0.5$  dex. One interpretation of this is that the increase in AGN feedback may be having a self-regulatory effect (Ni et al. 2023). Increasing AGN feedback strength more efficiently removes gas from the central regions, limiting the gas left to accrete, and driving down the total mass of the black hole over its lifetime (right panel of Figure 6). Integrating Equation 6 to obtain the total thermal energy that the AGN outputs over its lifetime, we find the energy output scales with  $A_{\text{AGN}}$ , but also the total (accreted) mass of the black hole such

that

$$E_{\text{AGN, lifetime}} = \epsilon_r A_{\text{AGN}} M_{\text{BH}} c^2. \quad (16)$$

Thus, higher values of  $A_{\text{AGN}}$  feedback would not output more total thermal energy over their lifetimes than lower values (shown explicitly in Appendix A, Figure 10). This limiting efficacy of AGN would also be consistent with the (slight) density enhancement seen in the inner regions in the top right panel of Figure 2.

## 4. DISCUSSION

### 4.1. Dark Matter-Only Simulations

As mentioned in Section 2.1, each hydrodynamic simulation in DREAMS has a corresponding DMO counterpart, which has the equivalent initial conditions. We can therefore make systematic comparisons on the im-

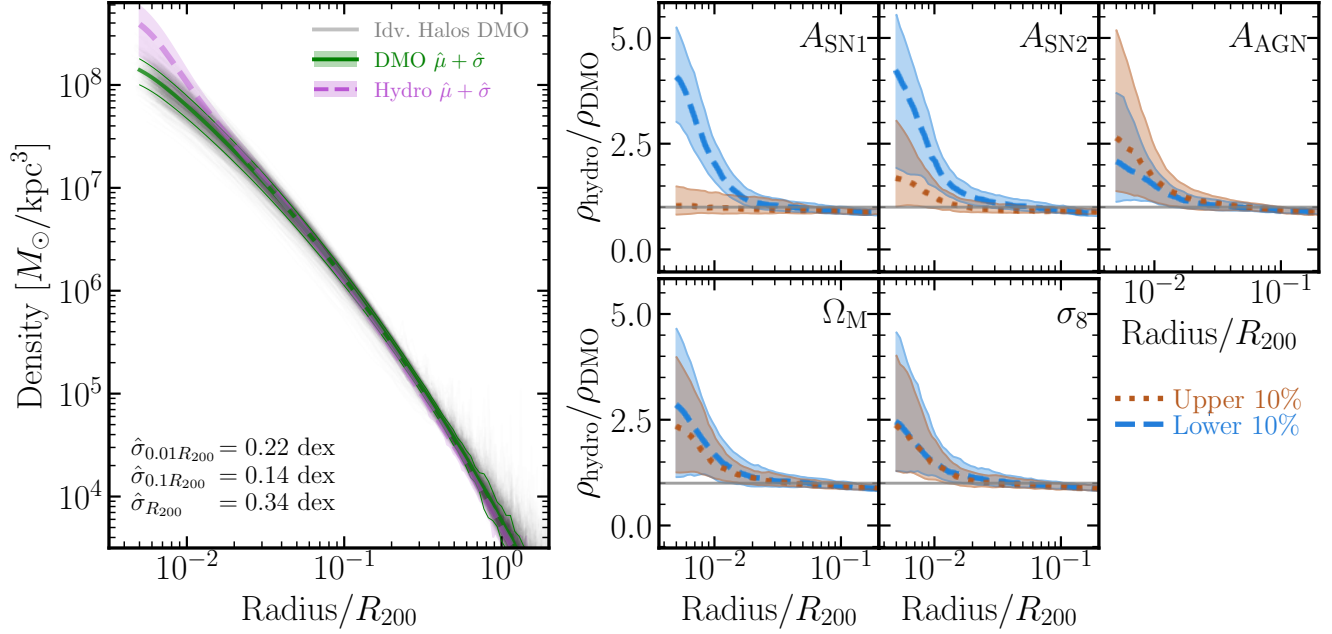


**Figure 7. Density Profiles from Dark Matter-Only Simulations.** Same as Figure 2, but for the Dark Matter-Only (DMO) simulations. The left-hand panel shows the DMO density profiles for each simulation normalized by  $R_{200}$ . The solid line and shaded regions being the weighted mean and standard deviation (see Section 2.4) from the DMO sims while the dashed line is the weighted mean and standard deviations from the hydro sims (i.e., the same as in Figure 2). The right-hand panels all show the ratio of the hydrodynamic simulations’ density to the corresponding DMO simulation for the same parameter ranges as the right-hand panels of Figure 2.

pect of baryons as a function of the varied parameters in the simulations (Figure 7).

The left-hand panel of Figure 7 shows the density profiles from the DMO DREAMS simulations. Each thin gray line is an individual halo, while the solid line and shaded region are the mean and standard deviation of the individual profiles. We quote weighted quantities in Figure 7 to be consistent with Figure 2, despite the baryonic feedback parameters not impacting the DMO simulations. As a point of reference, we also overplot the mean hydro density from Figure 2. The spread of the DMO density profiles is generally less than that of the hydro simulations in the inner radii but are roughly consistent at  $\gtrsim 0.1R_{200}$ . The spread at  $0.01R_{200}$  is 0.22 dex, which decreases to 0.14 dex at  $0.1R_{200}$  before increasing back to 0.34 dex at  $R_{200}$  radius due to the presence of subhalos. The spread across these radii is notably smaller than in the hydro simulations, further cementing the notion that the feedback variations are the dominant drivers of density profile variations in these inner regions. Moreover, the agreement at larger radii ( $> 0.1R_{200}$ ) further suggests that intrinsic halo-to-halo variations drive the scatter in this regime.

Each of the right-hand panels of Figure 7 shows the ratio of the hydro simulation density to the corresponding DMO simulation for different parameters (top left-

to-right:  $A_{\text{SN1}}$ ,  $A_{\text{SN2}}$ , and  $A_{\text{AGN}}$ , bottom left-to-right:  $\Omega_{\text{M}}$  and  $\sigma_8$ ). Similar to Figure 2, we show only the median predictions from the upper (dotted line) and lower (dashed line) 10% of each of the parameters for clarity. The shaded regions represent the 25<sup>th</sup> and 75<sup>th</sup> percentiles of the distributions.

In general, the density in the central region of the halo is significantly smaller for the DMO simulations relative to their hydro counterparts. The ratio of  $\rho_{\text{hydro}}$  to  $\rho_{\text{DMO}}$  at small radii ( $\lesssim 0.02R_{200}$ ) indicates a steeper inner profile in the hydro simulations (in agreement with the results of Section 3.2 and from in the EAGLE simulations Schaller et al. 2015). At larger radii ( $\gtrsim 0.1R_{200}$ ), the hydro and DMO profiles appear roughly consistent, though notably the hydro simulations have a slightly steeper outer slope (see, e.g.,  $\beta < 3$  in Section 3.2). The degree to which the density increases in the inner region is sensitive to the supernova feedback parameters. In particular, the supernova wind energy ( $A_{\text{SN1}}$ ) has a very strong impact relative to the DMO simulations. The low-range of  $A_{\text{SN1}}$  values lead to a factor of  $\sim 3$ –4 increase in the density compared to DMO, whereas the results for the high-range are roughly consistent with the DMO sims. This makes sense because the high-energy supernova should prevent baryon content from forming, leading to similar results as the DMO simulations. The

supernova wind speed ( $A_{\text{SN2}}$ ) shows a similar trend, albeit to a smaller extent, of increased feedback driving the density profiles closer to the DMO simulations. The upper 10% of  $\log(A_{\text{SN2}})$  increases the central density by only a factor of  $\sim 1.5$  on average, whereas the highest 10% change the density by a factor of  $> 4$ . On the other hand, the AGN feedback and cosmology variations do not have any significant impact relative to the DMO simulations.

We note that the ratio of  $\rho_{\text{hydro}}/\rho_{\text{DMO}}$  only rarely dips below unity in the inner radii of any of our halos, which contrasts results from the FIRE-2 simulations by [McKeown et al. \(2022\)](#), which find that the addition of baryon physics can suppress the inner density by factors of  $\sim 2$ . The difference between our work and [McKeown et al. \(2022\)](#) likely stems from the implementation of feedback in FIRE-2. One key difference in the FIRE model is the existence of strong, time-variable stellar feedback-driven winds ([Muratov et al. 2015](#)), which can perturb the galactic potential and “core” density profiles ([Governato et al. 2010](#); [Pontzen & Governato 2012](#); [Mostow et al. 2024](#)). We discuss the role of bursty feedback more in Section 4.2.1.

#### 4.2. Contraction of Dark Matter Halos

As mentioned in the 1, adiabatic contraction describes the dark matter’s response to baryons cooling within a halo. In short, as the baryons condense in the center of a galaxy, they also pull the dark matter particles inward, increasing their density in the central region. Since the DREAMS suite contains both DMO and hydrodynamic realizations of the same halo, it is natural to quantify whether the differences between the two are consistent with an adiabatically contracting halo.

[Blumenthal et al. \(1986\)](#) suggests that adiabatic contraction can be well approximated by a model with spherical symmetry, homologous contraction, and conservation of angular momentum. This approximation assumes that all dark matter particles are on circular orbits such that  $rM_{\text{enc}}(r)$  (where  $M_{\text{enc}}$  is the total mass enclosed at radius  $r$ ) is conserved upon infall.

In reality, dark matter can be on highly eccentric orbits (see, e.g., [Ghigna et al. 1998](#)), and  $rM_{\text{enc}}(r)$  is not an adiabatic invariant. In fact, the conserved quantities for eccentric orbits are the angular momentum *and* the radial action, which is non-zero. [Gnedin et al. \(2004\)](#) therefore extends the [Blumenthal et al. \(1986\)](#) model by showing that a better proxy for an invariant is  $rM_{\text{enc}}(\bar{r})$

$$\bar{r} = A \cdot R_{200} \left( \frac{r}{R_{200}} \right)^w, \quad (17)$$

where  $\bar{r}$  is the *orbit-averaged* radius for elliptical orbits and  $M(\bar{r})$  the mass enclosed within this radius. Here,

$A$  is a normalization constant and  $w$  is a slope (in log space) parameter that together control how the instantaneous orbital radius  $r$  is mapped onto its orbit-averaged value. These fit parameters are determined empirically on a halo-by-halo basis (see discussion in Appendix C)

The conservation of radial action can be written as

$$\begin{aligned} r_i \left[ M_{\text{DM},i}(\bar{r}_i) + M_{\text{baryon},i}(\bar{r}_i) \right] \\ = r_f \left[ M_{\text{DM},f}(\bar{r}_f) + M_{\text{baryon},f}(\bar{r}_f) \right], \end{aligned} \quad (18)$$

where  $M_{\text{DM}}$  is the enclosed dark matter mass and  $M_{\text{baryon}}$  is the enclosed baryonic mass at radius  $r$ , or average radius  $\bar{r}$ ,<sup>5</sup> in the initial (subscript  $i$ ) or final (subscript  $f$ ) state of the halo ([Gnedin et al. 2004](#); [Hussein et al. 2025](#)). The goal of this section is to create a mapping from  $M_{\text{DM},i}$  to  $M_{\text{DM},f}$ . We take the “initial” state of the system as the  $z = 0$  DMO simulation and the “final” state as the  $z = 0$  hydro simulation. In this way,  $M_{\text{DM},f}$  is exactly analogous to the mass-enclosed profile of the dark matter in the hydro simulation ( $M_{\text{DM}}^{\text{hydro}}$ ). We therefore predict  $M_{\text{DM}}^{\text{hydro}}$  given only the simplistic conservation of the action in Equation 18, referring to the result as  $M_{\text{DM}}^{\text{AC}}$ .

In practice, solving Equation 18 for  $M_{\text{DM}}^{\text{AC}}$  requires a few additional assumptions. For the term  $M_{\text{baryon},i}$  we assume that the “baryon component” of a DMO simulation follows a self-similar mass-enclosed profile to the dark matter ([Blumenthal et al. 1986](#); [Gnedin et al. 2004](#); [Binney & Tremaine 2008](#); [Hussein et al. 2025](#)). Then, we numerically solve Equation 18 using a fixed-point method. For each radius  $r_i$ , we solve for the corresponding contracted radius  $r_f$  by rearranging Equation 18 to obtain

$$r_f = r_i \left( \frac{M_{\text{DM}}^{\text{DMO}}(\bar{r}_i) \cdot f_{\text{norm}}(1 - f_b) + M_{\text{DM}}^{\text{DMO}}(\bar{r}_i) \cdot f_{\text{norm}}f_b}{M_{\text{DM}}^{\text{DMO}}(\bar{r}_i) \cdot f_{\text{norm}}(1 - f_b) + M_{\text{baryon}}^{\text{Hydro}}(\bar{r}_f)} \right), \quad (19)$$

where the ‘DMO’/‘Hydro’ superscript corresponds to the particular simulation that the enclosed mass per-

<sup>5</sup> Note that  $rM(\bar{r})$  is a mixed combination, as it is the product of the radius  $r$  and the mass enclosed within the orbit-averaged radius  $\bar{r}$ . Using a set of high-resolution collisionless simulations, [Gnedin et al. \(2004\)](#) showed that this combination is better conserved than  $\bar{r}M(\bar{r})$ .

tains to.<sup>6</sup> Here, the total enclosed mass of the DMO halo is rescaled by

$$f_{\text{norm}} = \frac{M_{\text{DM}}^{\text{Hydro}}(R_{200}) + M_{\text{baryon}}^{\text{Hydro}}(R_{200})}{M_{\text{DM}}^{\text{DMO}}(R_{200})}, \quad (21)$$

to ensure mass conservation with its hydro counterpart. The fraction of baryons is also obtained from the hydro simulation:

$$f_b = \frac{M_{\text{baryon}}^{\text{Hydro}}(R_{200})}{M_{\text{DM}}^{\text{Hydro}}(R_{200})}. \quad (22)$$

By rescaling the dark matter mass profile in the DMO simulation ( $M_{\text{DM}}^{\text{DMO}}$ ) by  $f_{\text{norm}}$  and  $f_b$ , we approximate the initial “baryon” component in the DMO simulation.

The denominator of Equation 19 depends on both the enclosed mass of the dark matter and baryon components in the hydro simulation. The latter is calculated directly at radius  $\bar{r}_f$ . The former is set by assuming

$$M_{\text{DM}}^{\text{AC}}(\bar{r}_f) = M_{\text{DM}}^{\text{DMO}}(\bar{r}_i). \quad (23)$$

Equation 23 ensures that the contraction proceeds in a strictly monotonic fashion, i.e., that shells of dark matter preserve their radial ordering and do not cross one another.

Equation 19 provides a map that relates each radius in the DMO simulation to its contracted counterpart in the hydrodynamic run. With this mapping from  $r_i$  to  $r_f$ , we use evaluate  $M_{\text{DM}}^{\text{DMO}}$  at  $r_f$  to determine our prediction  $M_{\text{DM}}^{\text{AC}}$ .

The main panel of Figure 8 shows the predictions for  $M_{\text{DM}}^{\text{AC}}$  as a function of radius normalized by the true  $M_{\text{DM}}^{\text{Hydro}}$ . From  $\sim 0.03R_{200}$  to  $R_{200}$ , the predicted adiabatically contracted profile is largely consistent with the hydro simulation. At smaller radii ( $\lesssim 0.02R_{200}$ ), however, the deviations are more notable, likely due to this region corresponding to the very center of the disk. Here, the effects of feedback are likely to be stronger due to, e.g., the higher concentration of supernovae relative to larger radii. Specifically, there is a significant under-prediction of the mass enclosed at  $\sim 0.01R_{200}$  and a subsequent over-prediction at radii  $< 0.01R_{200}$ . These

variations from the adiabatic contraction model start a few times  $10^{-2}R_{200}$  (a few kpc) from the center of the halo, which is where the galactic disk is likely to live. We therefore attribute the deviations at these small radii to the baryon feedback preventing the halo from contracting, or doing so adiabatically. Regardless, the bulk of the deviations from the adiabatic contraction model, at all radii, are mostly on the order of a few percent. Even in the most central regions, the predictions vary by  $\sim 3$ –10% from the hydro simulations. Overall, the agreement between predictions and simulation results suggests that the Gnedin et al. (2004) approximation for an adiabatically contracting halo with elliptical orbits is reasonable for the DREAMS halos.

A small fraction of halos (27) deviate significantly ( $\gg 10\%$ ) from the adiabatic contraction model at  $R_{200}$ . The large deviation at this radius is surprising considering that part of the calculation above is to renormalize the DMO profile based on masses at the virial radius (e.g., Equation 21). Upon further inspection, all of the cases where the profiles deviate significantly have a merger/large accretion event crossing the virial radius at  $z \sim 0$ . The exact timing of this event is different between the DMO and hydrodynamics simulations (which could be for a number of reasons, physical or numerical; Genel et al. 2019). The required renormalization of the DMO mass profile can therefore be systematically over- or under-estimated in situations where the infalling material crosses the virial radius at different times, leading to a failure of the adiabatically contracting halo model. Indeed, a halo undergoing a merger/large accretion event is likely to not be adiabatically (or even quasi-adiabatically) contracting (Velmani & Paranjape 2023).

#### 4.2.1. Comparison with Bursty Feedback Model

Virtually all of the DREAMS simulated halos agree with a simple adiabatically contracting model within  $\sim 10\%$  at all radii (Figure 8). This is in qualitative agreement with the findings of Hussein et al. (2025) who use the TNG (Pillepich et al. 2018a), AURIGA (Grand et al. 2017), and VINTERGATAN (Agertz et al. 2021; Rey et al. 2023) models. Importantly, TNG, AURIGA, and VINTERGATAN all model the star-forming interstellar medium (ISM) with an effective equation of state that results in smooth (i.e., non-bursty) stellar feedback (Springel & Hernquist 2003 for TNG and AURIGA and Agertz et al. 2013 for VINTERGATAN). It is worth reiterating that this is not a unique way to model the ISM. As mentioned in the Introduction, the FIRE model does have bursty feedback. Hussein et al. (2025) also made comparisons to the FIRE-2 model (Hopkins et al. 2018)

<sup>6</sup> Recall from Section 2.1 that the DMO simulations include an  $\Omega_b$  fraction of baryons, which are treated as collisionless particles. This additional collisionless mass effectively increases the total dark matter mass in the DMO simulations by  $\Omega_b$ . To account for this “extra” mass, we make the following correction:

$$M_{\text{DM}}^{\text{DMO, corrected}} = M_{\text{DM}}^{\text{DMO}} \times \left( \frac{\Omega_{\text{M}} - \Omega_b}{\Omega_{\text{M}}} \right), \quad (20)$$

where  $M_{\text{DM}}^{\text{DMO}}$  is the mass-enclosed profile for the DMO simulation. From this point onwards, we refer to the “corrected” quantity when referencing  $M_{\text{DM}}^{\text{DMO}}$ .



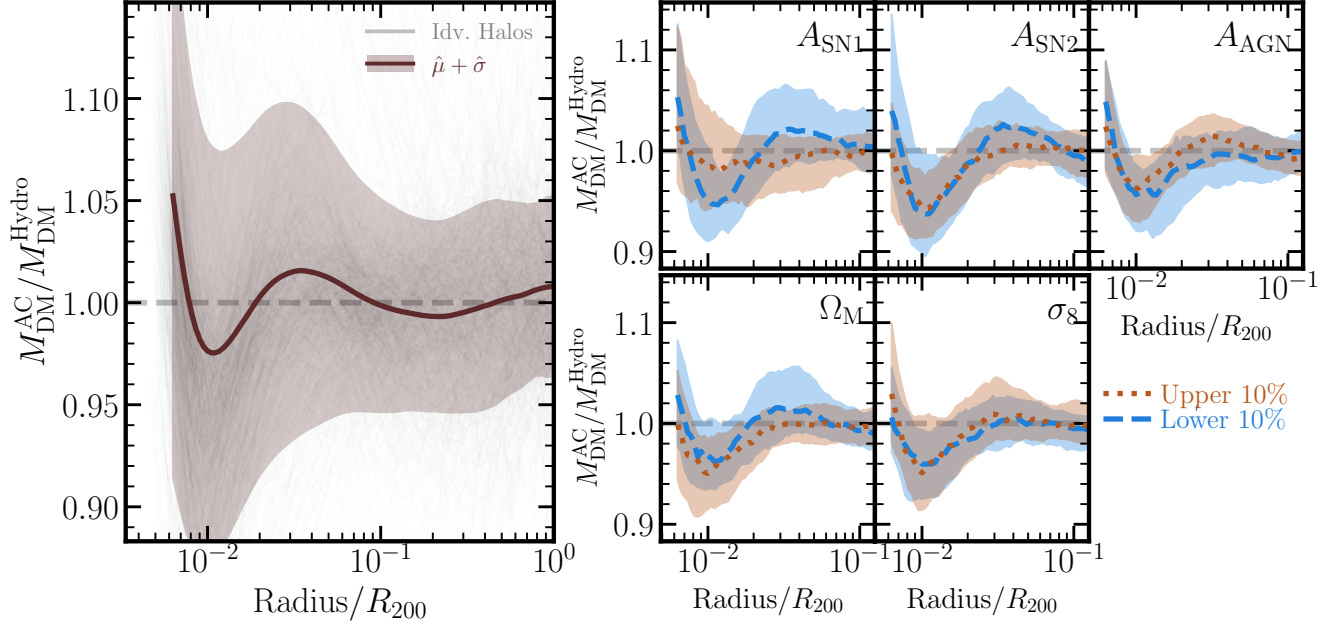


**Figure 8. Ratio of Estimated Mass Contraction to Hydrodynamic Simulation Mass Profiles.** The ratio of the predicted adiabatically contracted dark matter mass profile ( $M_{\text{DM}}^{\text{AC}}$ ; using the methods outlined in [Gnedin et al. 2004](#)) to the dark matter mass profile of the full hydrodynamic simulations ( $M_{\text{DM}}^{\text{Hydro}}$ ). The solid line represents the weighted mean of the distribution, while the shaded region is the weighted spread (see Section 2.4). The level to which the halos agree with the adiabatically contracting halo model is mostly independent of astrophysics or cosmology parameter variations at radii  $\gtrsim 0.03R_{200}$  (with the exception of  $A_{\text{SN1}}$ ).

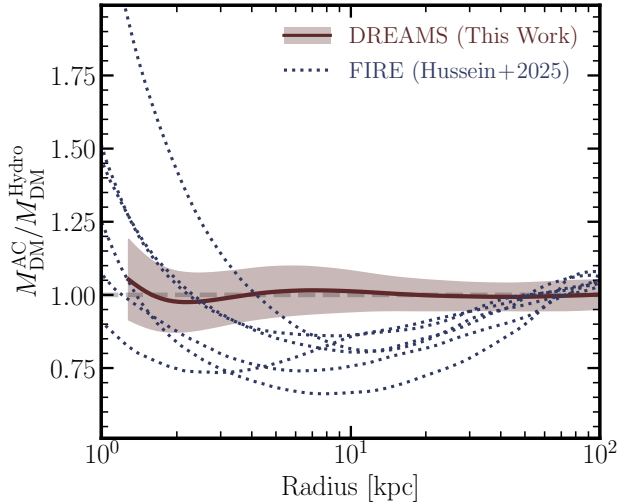


**Figure 9. Role of Bursty Feedback in Adiabatic Contraction.** The ratio between the DM mass predicted using adiabatic contraction (using [Gnedin et al. 2004](#)) and the DM mass in hydro sims. Shown here for both FIRE-2 (data from [Hussein et al. 2025](#); note that each line is an individual halo) and DREAMS (same as Figure 8 without radial normalization). The *bursty* feedback model, FIRE, varies far more significantly than even the strongest feedback models in DREAMS. This suggests that variations from adiabatic contraction are driven by bursty feedback and not just strong feedback.

and find that the FIRE model varies significantly (factors of  $\gtrsim 2$ ; shown in Figure 9) from the simple case of an adiabatically contracting halo. Figure 9 demonstrates that the element of the FIRE model that is causing the deviations from adiabatic contraction is the *bursty* feedback—not just strong feedback. As we showed in the previous subsection, the feedback variations in the TNG model are sufficiently strong to almost entirely prevent the build up of a stellar component in the galaxy; however, the TNG model does not have bursty feedback. Variations from an adiabatically contracting halo in even the most extreme TNG feedback variations are significantly less than those of FIRE-2, suggesting that bursty, episodic feedback plays the strongest role setting deviations from the adiabatically contracting halo.

## 5. CONCLUSION

In this work, we investigated the impact of variations in the IllustrisTNG physical model and cosmology on the dark matter density profiles of Milky Way-mass halos using the DREAMS simulations. The DREAMS CDM suite consists of 1024 hydrodynamic simulations with variations in supernova feedback, AGN feedback, and cosmology (see, e.g., Figure 1 for a few such halos) as well as a corresponding set of 1024 DMO simulations. These simulation suites enabled us to quantify the role that baryons play in the assembly of dark matter halos.

Our conclusions are as follows:

- Overall, we find that there are only minor variations in the density profiles of Milky Way-mass halos with variations to the IllustrisTNG model (Section 3.1 Figure 2). Virtually all variation in the density profiles is driven by halo-to-halo variation, with a relatively small contribution from our two supernova parameters (which only create differences of  $\pm \sim 20 - 50\%$  in the inner regions— $< 0.01R_{200}$ —of the halos).
- We fit the density profiles with a generalized NFW profile (e.g., Jaffe 1983; Hernquist 1990) which has two normalization free parameters and three shape parameters (Equation 9, Section 3.2). We, again, find that intrinsic halo-to-halo variations plays the dominant role in setting both the normalization and shape of halos. Beyond the halo-to-halo variance, we find that changes to the supernova wind speed ( $A_{\text{SN}2}$ ) can also vary the normalization of the profile (Figure 3) and increases to the wind energies ( $A_{\text{SN}1}$ ) can drive the shape of the profiles closer to NFW (Figure 4). Physically, this suggests that ejecting *faster* winds may have a stronger disruption of the potential, whereas *more* wind energy more effectively suppresses stellar mass growth.
- We then quantify how much each halo mass increases using the central mass growth: the ratio of the DMO simulation mass enclosed to the hydro simulation mass enclosed at  $0.01R_{200}$  (Figure 5). Here, we find that the astrophysics variations play a dominant role. Larger values of  $A_{\text{SN}1}$  and  $A_{\text{SN}2}$  are more efficient at preventing stellar mass growth (left two panels of Figure 6), thus the halo contracts less. On the other hand, we find the opposite trend in  $A_{\text{AGN}}$ : increasing black hole feedback increases the work required to contract (right panel of Figure 6, see also Appendix A).
- We compare the results of the hydro simulations to DMO simulations with matched initial conditions (Section 4.1). On the whole, we find that the DMO simulations have a lower density in the inner regions ( $\lesssim 0.01R_{200}$ ) than the hydro simulations (Figure 7). The extent to which the density is larger depends on the feedback, however. In fact, we find that lower values of  $A_{\text{SN}1}$  tend towards a ratio of unity with respect to the DMO simulations, in good agreement with the results of the shape of the profiles and stellar mass growth.
- We quantify whether or not our halos are consistent with approximations to adiabatic contraction (Section 4.2). We find that halos generally agree within

$\sim 10\%$  regardless of the feedback or cosmology (Figure 8); however, systems with late-time mergers that occur at slightly different times between the hydro and DMO simulations tend to disagree significantly. As with many previous results, we find that the supernova wind energy changes the picture due to the lack of baryon mass accumulation: these halos contract adiabatically at virtually all radii.

- Finally, we show that the bursty feedback FIRE(-2) model produces significantly larger deviations from adiabatic contraction than any feedback variation in the TNG model (Figure 9). This suggests that what drives deviations from adiabatic contractions are *bursts* of stellar feedback, not just strong feedback.

Taken together, these results show that halo-to-halo variance is the dominant source of scatter in Milky Way-mass dark matter profiles in the TNG model, with SN1 and SN2 feedback parameters producing secondary but non-negligible effects. AGN feedback plays a smaller role, and cosmological parameter variations are essentially irrelevant at this mass scale.

Understanding and quantifying the range of predictions in an individual simulation model is a difficult task, yet it is necessary to fully understand that model. This work, which is part of a broader series in the DREAMS project, represents one such investigation into the sensitivity of the TNG model to its input physics within a  $\Lambda$ CDM context. Such a benchmark is useful in the wider landscape of future simulation efforts to vary different simulation models, feedback physics, and dark matter physics within the DREAMS collaboration. The quantification of the range of density profiles in the IllustrisTNG model has implications for dark matter indirect detection experiments using the Galactic center, which we plan to explore in more detail in a companion work (A.M. Garcia et al. In Preparation).

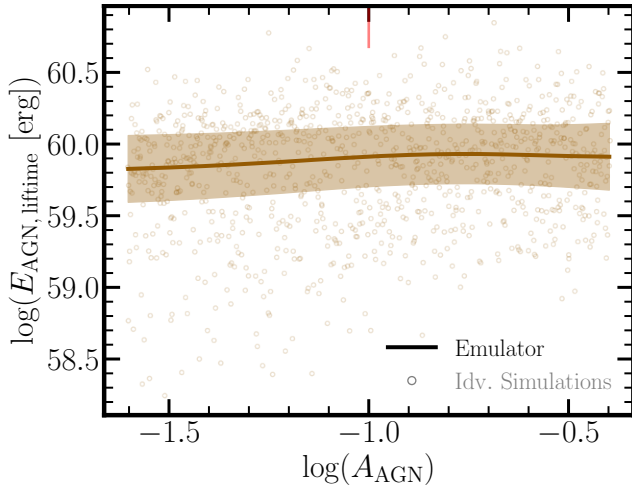


**Figure 10. Approximate AGN Feedback Budget** The approximated lifetime feedback energy of the AGN (via Equation 16) in each simulation (open circles). The solid line (and shaded region thereof) represents the predictions from an ensemble of emulators.

#### A. ASSESSING THE ROLE OF $A_{\text{AGN}}$

As mentioned a number of times in the main text, we find interesting trends between physical properties of the halo and the AGN feedback. In Section 3.3, we lay out an argument for these trends based on an approximation of the total feedback energy (by integrating Equation 6; see also a similar argument made by Ni et al. 2023). In

The authors acknowledge Research Computing at The University of Virginia for providing computational resources and technical support that have contributed to the results reported within this publication. URL: <https://rc.virginia.edu>.

AMG acknowledges a helpful conversation with Sebastian Trujillo-Gomez as a part of the Simulation Based Inference Conference. AMG also acknowledges a helpful conversation with Aklant Bhowmick regarding fitting gNFW profiles. AMG thanks Carrie Filion for helpful comments that led to the success of this work. Finally, AMG acknowledges Kate Garcia for assistance in the design of Figure 1 and Kelly Garcia for assistance in the design of Figure 4.

AMG and PT acknowledge support from the National Science Foundation under Cooperative Agreement 2421782 and the Simons Foundation grant MPS-AI-00010515 awarded to NSF-Simons AI Institute for Cosmic Origins — CosmicAI, <https://www.cosmicai.org/>

#### APPENDIX

this appendix, we show how the mass of the central black hole and this approximation for feedback energy scale with  $A_{\text{AGN}}$  as well as offer a brief physical argument for the saturation.

Figure 10 shows the central black hole mass for each DREAMS halo as a function of  $A_{\text{AGN}}$  (open circles in top panel) as well as our approximation for the total feedback energy imparted by that black hole (via Equation 16; open circles in bottom panel). In addition, we train a series of emulators (see Section 2.3) and report the aggregate predictions in the solid line and shaded region. We find that the black hole mass decreases with increasing  $A_{\text{AGN}}$ . The rate of black hole mass decrease speeds up with increasing  $A_{\text{AGN}}$ . The reason for this is that the AGN become more effective at removing gas from the central regions with increasing  $A_{\text{AGN}}$ , thereby curtailing the total mass accretion onto the central black hole. Furthermore, we find that when solving Equation 16 using this central black hole mass, we find that the total feedback energy over the life time of the black hole is virtually unchanged ( $\sim 10^{60}$  erg) by variations in  $A_{\text{AGN}}$ . There is a *slight* increase in feedback energy at values less than the fiducial TNG values ( $\log[A_{\text{AGN}}] \lesssim -1$ ), but it is completely flat above the fiducial value. This suggests that the total work that the AGN does (in the thermal mode) is roughly constant as a function of  $A_{\text{AGN}}$ .

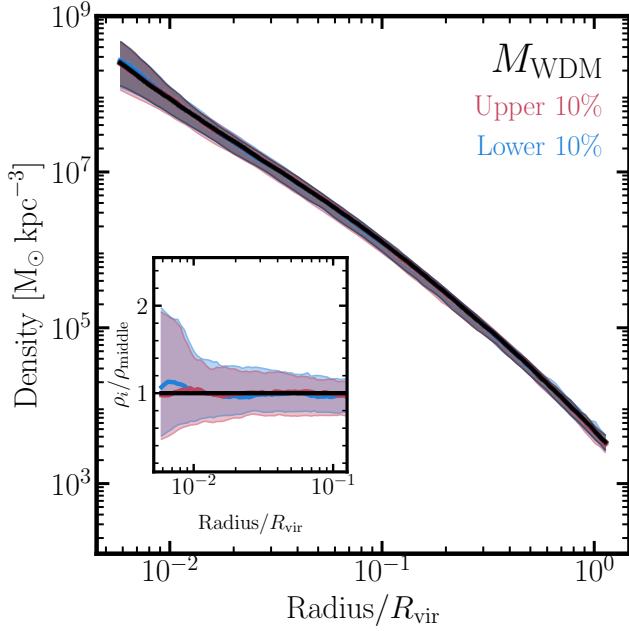


**Figure 11. Density Profiles in the DREAMS Warm Dark Matter Milky Way mass suite.** Similar to Figure 2 but for the WDM suite variations of WDM particle mass ( $M_{\text{WDM}}$ ). We note that  $M_{\text{WDM}}$  is sampled inversely ( $1/M_{\text{WDM}}$ ).

We can write a toy model for the balance of feedback from the AGN with the accretion onto the black hole by equating the energy via feedback to the binding energy of the surrounding gas. We can approximate the system in equilibrium with given Equation 16 and the gravitational binding energy of the gas such that

$$A_{\text{AGN}} \epsilon_r M_{\text{BH}} c^2 \approx G \frac{M_{\text{gas}}^2}{r}, \quad (\text{A1})$$

where  $M_{\text{gas}}$  is the mass of gas within a radius  $r$  of the black hole. We can then rearrange Equation A1 to find  $M_{\text{BH}} \propto A_{\text{AGN}}^{-1}$ . While a crude and incomplete physical picture of the complexities of the center of galaxies which lay host to AGN, it is interesting to note that the inverse scaling of  $M_{\text{BH}}$  with increasing  $A_{\text{AGN}}$  is in broad agreement with the trends we find in the DREAMS simulations (Figure 10).

### B. (LACK OF) VARIATIONS DUE TO WARM DARK MATTER PARTICLE MASS

The DREAMS suite also provides a suite of 1024 Milky Way mass halos with Warm Dark Matter (WDM) in addition to the CDM suite of Milky Way mass galaxies. The focus of the above analysis is solely on the CDM suite; however, an equivalent analysis could be performed using the WDM simulations instead. In this

Appendix, we briefly examine the impact of WDM on Milky Way mass halos in DREAMS.

The WDM suite of galaxies is very similar to that of CDM suite with a few key exceptions. Here we briefly note any such differences between the two (and refer the reader to Rose et al. 2025 for the complete reference on the WDM suite). The most important difference between the WDM and CDM suites is the difference in dark matter. To simulate a WDM universe, DREAMS makes modifications to the initial matter power spectrum (following from Bode et al. 2001) such that  $P_{\text{WDM}} = \beta(k) P_{\text{CDM}}$  where

$$\beta(k) = \left[ (1 + (\alpha k)^{2.4})^{-5.0/1.2} \right]^2 \quad \text{and} \quad (\text{B2})$$

$$\alpha = 0.048 \left( \frac{M_{\text{WDM}}}{\text{keV}} \right)^{-1.15} \left( \frac{\Omega_{\text{M}} - \Omega_{\text{b}}}{0.4} \right)^{0.15} \left( \frac{h}{0.65} \right)^{1.3}, \quad (\text{B3})$$

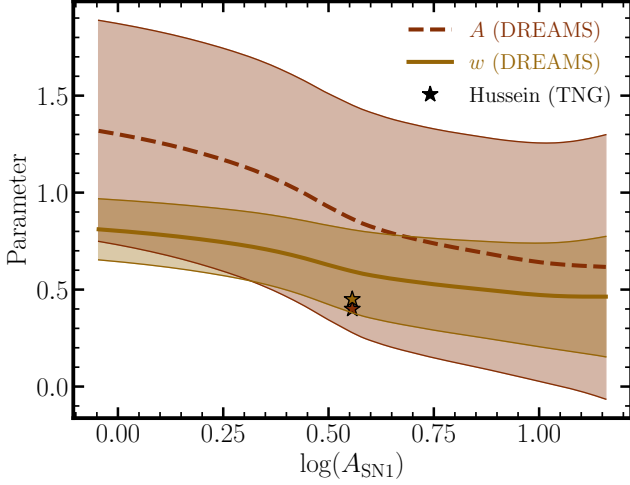
where  $k$  is the wavenumber (inverse scale) and  $M_{\text{WDM}}$  is the desired WDM particle mass. In the limit that  $M_{\text{WDM}} \rightarrow \infty$ ,  $P_{\text{WDM}} \rightarrow P_{\text{CDM}}$ . The WDM particle mass,  $M_{\text{WDM}}$ , is varied according to a Sobol' (1967) sequence in  $1/M_{\text{WDM}}$  space from 1.8 keV to 30 keV. We also that  $\Omega_{\text{M}}$  and  $\sigma_8$  are fixed in the WDM suite, whereas  $A_{\text{SN1}}$ ,  $A_{\text{SN2}}$ , and  $A_{\text{AGN}}$  are varied in the same manner as listed in Table 1.

Figure 11 shows the summary of dark matter density profiles for all of the DREAMS WDM galaxies. On the whole, we find that the halo-to-halo variation is very similar between the CDM and WDM suites. We find that variations in the WDM particle mass have no systematic effect on the dark matter density of Milky Way mass halos. We therefore conclude that virtually all of the analysis performed in the main body of this work would be practically unchanged by variations in the WDM particle mass. Indeed, the lack of importance on WDM is expected based the WDM suppressing power on scales much smaller than those of the Milky Way mass halos.

### C. ADIABATIC CONTRACTION FIT PARAMETERS

As mentioned in Section 4.2, the Gnedin et al. (2004) adiabatic contraction model includes a best-fit parameterization of the orbit-averaged radius  $\bar{r}$  (Equation 17). The free parameters,  $A$  and  $w$  (corresponding to a normalization and exponent of the fit), in our work are determined on a halo-by-halo basis. Not every work follows this practice of fitting  $A$  and  $w$  on a halo-by-halo basis is non-standard, however. For example, Hussein et al. (2025) report fit their halos using the *average*  $A$  and  $w$  parameters. We opt to not use the average values of  $A$





**Figure 12. Distribution of  $A$  and  $w$  parameters from DREAMS simulations.** Predictions from our emulators for the best fit  $A$  and  $w$  values (from Equation 17) as a function of  $A_{\text{SNI}}$  (we note that  $A$  and  $w$  do not depend sensitively on any other DREAMS simulation parameter). The stars correspond to the average values from Hussein et al. (2025;  $A = 0.40$  and  $w = 0.45$ ), which fall well within the halo-to-halo variation of our predictions.

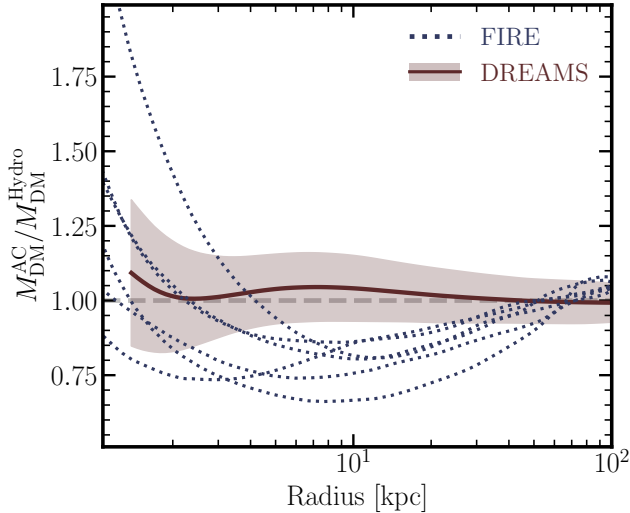


**Figure 13. Ratio of Mass Contraction to Hydrodynamic Simulation Mass Profiles using fixed  $A$  and  $w$ .** Same as Figure 9, but assuming a fixed  $A$  and  $w$  value of the average of the DREAMS distribution ( $A = 0.848$  and  $w = 0.675$ ). We still find qualitatively different behavior between FIRE-2 and DREAMS.

and  $w$  since we find that they have a dependency on the physics variations that DREAMS employs. In particular, we find that both  $A$  and  $w$  depend on  $A_{\text{SNI}}$  (Figure 12). With increasing  $A_{\text{SNI}}$ , both  $A$  and  $w$  decrease (though the former more so than the later). These trends follow fairly closely to those observed with the

central mass growth show in Figure 5, i.e., halos that undergo more contraction have larger  $A$  and  $w$  values, which physically correspond to systematically smaller orbit-averaged radii, indicating that dark matter particles have moved deeper into the potential well.

We note, however, that if we instead were to use the average values of  $A = 0.848$  and  $w = 0.675$  our results are qualitatively unchanged.<sup>7</sup> Figure 13 shows the resulting predicted adiabatic contraction profiles by instead fixing  $A$  and  $w$ . On average, we find slightly worse agreement between our adiabatic contraction model and the true hydrodynamic simulations, but the level to which the two disagree is within  $\sim 10\%$ . Moreover, we find that the (weighted) scatter also increases when considering fixed  $A$  and  $w$ . Our key conclusion about the comparison between the bursty feedback model FIRE remains qualitatively unchanged, however. Even with fitting halos with poorly constrained  $A$  and  $w$  values given their particular physics implementation, we find that the deviations seen in FIRE halos are significantly larger than those of the DREAMS halos.

#### D. EMULATOR VALIDATION TEST

As mentioned in Section 2.3, we build a series of neural network emulators to help support the findings of this work. Each time we build an emulator (Figures 3, 4, 5, 6, 10, and 12), we verify the model by comparing the predictions of the model to the raw simulation outputs (following from Rose et al. 2025). We show Figure 14 as an example of this validation process. The left hand panel of Figure 14 is identical to Figure 4 with the addition of the true rolling mean (solid line) and standard deviation (gray shaded region) from these measured simulation data points. One potential reason for a small amount of disagreement would be that our emulator is trained to predict single parameter dependencies (i.e., we keep all other parameters fixed), whereas the raw simulation outputs have co-variation of parameters. In order to capture this co-variance, we would need a slightly different architecture, such as normalizing flows (see, e.g., E. Lille In Prep). Regardless, we find that the emulated prediction for the mean is largely consistent with these raw simulation outputs even with out simple emulator. Figure 14 further demonstrates the utility of the emulator: the true rolling median is significantly noisier than the predictions from the emulated sample.

<sup>7</sup> We note that these average values of  $A$  and  $w$  are different than those reported in Hussein et al. (2025;  $A = 0.40$  and  $w = 0.45$ ), who use six halos in the TNG model (albeit without the physics variations). However, we find that the Hussein et al. (2025) values are consistent with our results within the halo-to-halo variation (shown as the stars in Figure 12).

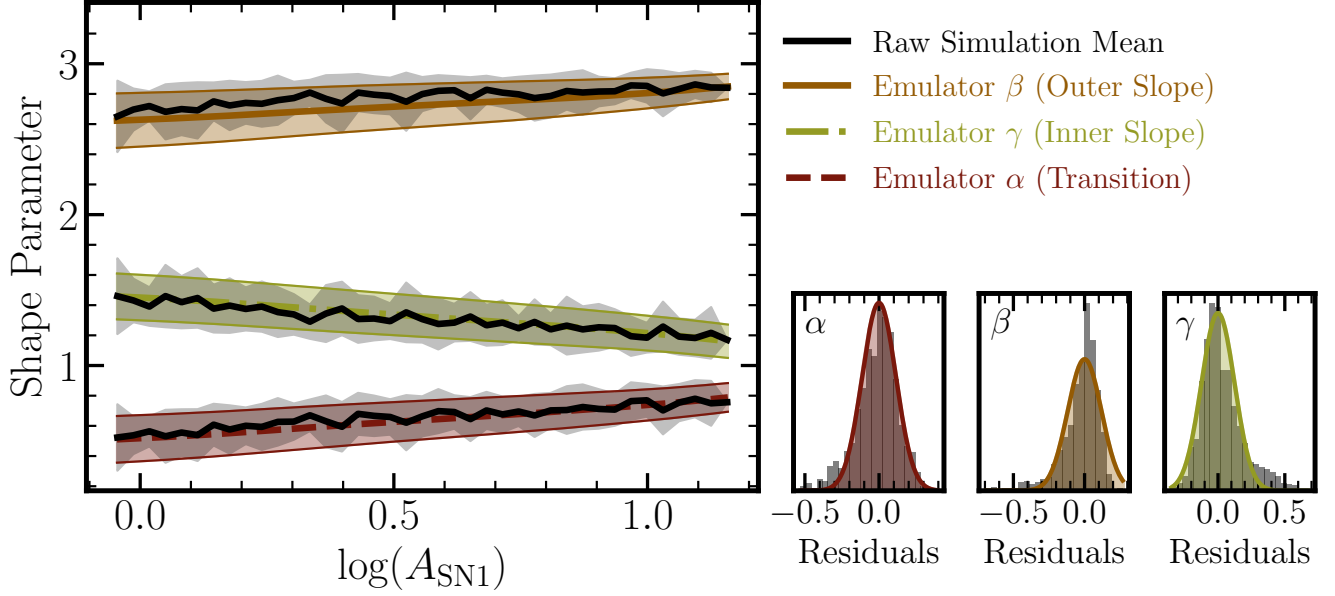


**Figure 14. Example Emulator Validation** *Left:* Same as Figure 4, with the raw estimate of the rolling mean and standard deviation (solid line and gray shaded region) for each parameter. *Right:* Histograms of the residuals about the true median for  $\alpha$  (left),  $\beta$  (middle), and  $\gamma$  (right) along with the distributions showing the a Gaussian distribution consistent with the average standard deviation predicted by the emulator.

The right hand panels of Figure 14 show the distribution of raw residuals compared to an average estimate from the emulator. We note that the scatter about the shape parameters can vary as a function of  $A_{\text{SNI}}$  in both the raw dataset and emulator; however, for the purposes here we compare the full distribution of residuals against the average of the standard deviations from the emulator. There is some level of disagreement in the tails of

the distributions (in particular in  $\gamma$ ), which, again, could be more effectively captured with a more sophisticated architecture, but for the most part we find that the standard deviation of the datasets match quite well with the raw simulation data.

We perform the same test for each of the emulators built in this work and find a similar level agreement.

## REFERENCES

- Abadi, M. G., Navarro, J. F., Fardal, M., Babul, A., & Steinmetz, M. 2010, *MNRAS*, 407, 435, doi: [10.1111/j.1365-2966.2010.16912.x](https://doi.org/10.1111/j.1365-2966.2010.16912.x)
- Agertz, O., Kravtsov, A. V., Leitner, S. N., & Gnedin, N. Y. 2013, *ApJ*, 770, 25, doi: [10.1088/0004-637X/770/1/25](https://doi.org/10.1088/0004-637X/770/1/25)
- Agertz, O., Renaud, F., Feltzing, S., et al. 2021, *MNRAS*, 503, 5826, doi: [10.1093/mnras/stab322](https://doi.org/10.1093/mnras/stab322)
- Akiba, T., Sano, S., Yanase, T., Ohta, T., & Koyama, M. 2019, in *Proceedings of the 25th ACM SIGKDD International Conference on Knowledge Discovery & Data Mining, KDD '19 (New York, NY, USA: Association for Computing Machinery)*, 2623–2631, doi: [10.1145/3292500.3330701](https://doi.org/10.1145/3292500.3330701)
- Bhagwat, A., Costa, T., Ciardi, B., Pakmor, R., & Garaldi, E. 2024, *MNRAS*, 531, 3406, doi: [10.1093/mnras/stae1125](https://doi.org/10.1093/mnras/stae1125)
- Binney, J., & Tremaine, S. 2008, *Galactic Dynamics: Second Edition* (Princeton University Press)
- Blumenthal, G. R., Faber, S. M., Flores, R., & Primack, J. R. 1986, *ApJ*, 301, 27, doi: [10.1086/163867](https://doi.org/10.1086/163867)
- Bode, P., Ostriker, J. P., & Turok, N. 2001, *ApJ*, 556, 93, doi: [10.1086/321541](https://doi.org/10.1086/321541)
- Brooks, A. M., & Zolotov, A. 2014, *ApJ*, 786, 87, doi: [10.1088/0004-637X/786/2/87](https://doi.org/10.1088/0004-637X/786/2/87)
- Bullock, J. S., & Boylan-Kolchin, M. 2017, *ARA&A*, 55, 343, doi: [10.1146/annurev-astro-091916-055313](https://doi.org/10.1146/annurev-astro-091916-055313)
- Callingham, T. M., Cautun, M., Deason, A. J., et al. 2019, *MNRAS*, 484, 5453, doi: [10.1093/mnras/stz365](https://doi.org/10.1093/mnras/stz365)
- Cautun, M., Benítez-Llambay, A., Deason, A. J., et al. 2020, *MNRAS*, 494, 4291, doi: [10.1093/mnras/staa1017](https://doi.org/10.1093/mnras/staa1017)
- Chabrier, G. 2003, *PASP*, 115, 763, doi: [10.1086/376392](https://doi.org/10.1086/376392)
- Chan, T. K., Kereš, D., Oñorbe, J., et al. 2015, *MNRAS*, 454, 2981, doi: [10.1093/mnras/stv2165](https://doi.org/10.1093/mnras/stv2165)

- Chua, K. T. E., Pillepich, A., Vogelsberger, M., & Hernquist, L. 2019, *MNRAS*, 484, 476, doi: [10.1093/mnras/sty3531](https://doi.org/10.1093/mnras/sty3531)
- Chua, K. T. E., Vogelsberger, M., Pillepich, A., & Hernquist, L. 2022, *MNRAS*, 515, 2681, doi: [10.1093/mnras/stac1897](https://doi.org/10.1093/mnras/stac1897)
- Crain, R. A., & van de Voort, F. 2023, *ARA&A*, 61, 473, doi: [10.1146/annurev-astro-041923-043618](https://doi.org/10.1146/annurev-astro-041923-043618)
- Curti, M., Mannucci, F., Cresci, G., & Maiolino, R. 2020, *MNRAS*, 491, 944, doi: [10.1093/mnras/stz2910](https://doi.org/10.1093/mnras/stz2910)
- de Blok, W. J. G. 2010, *Advances in Astronomy*, 2010, 789293, doi: [10.1155/2010/789293](https://doi.org/10.1155/2010/789293)
- de Blok, W. J. G., & Bosma, A. 2002, *A&A*, 385, 816, doi: [10.1051/0004-6361:20020080](https://doi.org/10.1051/0004-6361:20020080)
- de Blok, W. J. G., Walter, F., Brinks, E., et al. 2008, *AJ*, 136, 2648, doi: [10.1088/0004-6256/136/6/2648](https://doi.org/10.1088/0004-6256/136/6/2648)
- Dekel, A., & Silk, J. 1986, *ApJ*, 303, 39, doi: [10.1086/164050](https://doi.org/10.1086/164050)
- Di Cintio, A., Brook, C. B., Dutton, A. A., et al. 2014, *MNRAS*, 441, 2986, doi: [10.1093/mnras/stu729](https://doi.org/10.1093/mnras/stu729)
- Duffy, A. R., Schaye, J., Kay, S. T., et al. 2010, *MNRAS*, 405, 2161, doi: [10.1111/j.1365-2966.2010.16613.x](https://doi.org/10.1111/j.1365-2966.2010.16613.x)
- EGGEN, O. J., LYNDEN-BELL, D., & SANDAGE, A. R. 1962, *ApJ*, 136, 748, doi: [10.1086/147433](https://doi.org/10.1086/147433)
- Fall, S. M., & Efstathiou, G. 1980, *MNRAS*, 193, 189, doi: [10.1093/mnras/193.2.189](https://doi.org/10.1093/mnras/193.2.189)
- Feldmann, R., & Bieri, R. 2025, arXiv e-prints, arXiv:2507.08925. <https://arxiv.org/abs/2507.08925>
- Fitts, A., Boylan-Kolchin, M., Elbert, O. D., et al. 2017, *MNRAS*, 471, 3547, doi: [10.1093/mnras/stx1757](https://doi.org/10.1093/mnras/stx1757)
- Font, A. S., McCarthy, I. G., Poole-Mckenzie, R., et al. 2020, *MNRAS*, 498, 1765, doi: [10.1093/mnras/staa2463](https://doi.org/10.1093/mnras/staa2463)
- Foreman-Mackey, D., Hogg, D. W., Lang, D., & Goodman, J. 2013, *PASP*, 125, 306, doi: [10.1086/670067](https://doi.org/10.1086/670067)
- Garcia, A. M., Torrey, P., Hemler, Z. S., et al. 2023, *MNRAS*, 519, 4716, doi: [10.1093/mnras/stac3749](https://doi.org/10.1093/mnras/stac3749)
- Garcia, A. M., Torrey, P., Ellison, S., et al. 2024a, *MNRAS*, 531, 1398, doi: [10.1093/mnras/stae1252](https://doi.org/10.1093/mnras/stae1252)
- Garcia, A. M., Torrey, P., Grasha, K., et al. 2024b, *MNRAS*, 529, 3342, doi: [10.1093/mnras/stae737](https://doi.org/10.1093/mnras/stae737)
- Garcia, A. M., Torrey, P., Bhagwat, A., et al. 2025a, arXiv e-prints, arXiv:2503.03804, doi: [10.48550/arXiv.2503.03804](https://doi.org/10.48550/arXiv.2503.03804)
- Garcia, A. M., Torrey, P., Ellison, S. L., et al. 2025b, *MNRAS*, 536, 119, doi: [10.1093/mnras/stae2587](https://doi.org/10.1093/mnras/stae2587)
- Genel, S., Bryan, G. L., Springel, V., et al. 2019, *ApJ*, 871, 21, doi: [10.3847/1538-4357/aaf4bb](https://doi.org/10.3847/1538-4357/aaf4bb)
- Ghigna, S., Moore, B., Governato, F., et al. 1998, *MNRAS*, 300, 146, doi: [10.1046/j.1365-8711.1998.01918.x](https://doi.org/10.1046/j.1365-8711.1998.01918.x)
- Gnedin, O. Y., Kravtsov, A. V., Klypin, A. A., & Nagai, D. 2004, *ApJ*, 616, 16, doi: [10.1086/424914](https://doi.org/10.1086/424914)
- Governato, F., Brook, C., Mayer, L., et al. 2010, *Nature*, 463, 203, doi: [10.1038/nature08640](https://doi.org/10.1038/nature08640)
- Grand, R. J. J., Gómez, F. A., Marinacci, F., et al. 2017, *MNRAS*, 467, 179, doi: [10.1093/mnras/stx071](https://doi.org/10.1093/mnras/stx071)
- Greene, J. E., Strader, J., & Ho, L. C. 2020, *ARA&A*, 58, 257, doi: [10.1146/annurev-astro-032620-021835](https://doi.org/10.1146/annurev-astro-032620-021835)
- Hartley, B., & Ricotti, M. 2016, *MNRAS*, 462, 1164, doi: [10.1093/mnras/stw1562](https://doi.org/10.1093/mnras/stw1562)
- Hernquist, L. 1990, *ApJ*, 356, 359, doi: [10.1086/168845](https://doi.org/10.1086/168845)
- Hopkins, P. F., Kereš, D., Oñorbe, J., et al. 2014, *MNRAS*, 445, 581, doi: [10.1093/mnras/stu1738](https://doi.org/10.1093/mnras/stu1738)
- Hopkins, P. F., Wetzel, A., Kereš, D., et al. 2018, *MNRAS*, 480, 800, doi: [10.1093/mnras/sty1690](https://doi.org/10.1093/mnras/sty1690)
- Huang, Y., Liu, X. W., Yuan, H. B., et al. 2016, *MNRAS*, 463, 2623, doi: [10.1093/mnras/stw2096](https://doi.org/10.1093/mnras/stw2096)
- Hussein, A., Necib, L., Kaplinghat, M., et al. 2025, arXiv e-prints, arXiv:2501.14868, doi: [10.48550/arXiv.2501.14868](https://doi.org/10.48550/arXiv.2501.14868)
- Jaffe, W. 1983, *MNRAS*, 202, 995, doi: [10.1093/mnras/202.4.995](https://doi.org/10.1093/mnras/202.4.995)
- Jahn, E. D., Sales, L. V., Marinacci, F., et al. 2023, *MNRAS*, 520, 461, doi: [10.1093/mnras/stad109](https://doi.org/10.1093/mnras/stad109)
- Jeffrey, N., & Wandelt, B. D. 2020, arXiv e-prints, arXiv:2011.05991, doi: [10.48550/arXiv.2011.05991](https://doi.org/10.48550/arXiv.2011.05991)
- Kugel, R., Schaye, J., Schaller, M., et al. 2023, *MNRAS*, 526, 6103, doi: [10.1093/mnras/stad2540](https://doi.org/10.1093/mnras/stad2540)
- Larson, R. B. 1974, *MNRAS*, 169, 229, doi: [10.1093/mnras/169.2.229](https://doi.org/10.1093/mnras/169.2.229)
- Lazar, A., Bullock, J. S., Boylan-Kolchin, M., et al. 2020, *MNRAS*, 497, 2393, doi: [10.1093/mnras/staa2101](https://doi.org/10.1093/mnras/staa2101)
- Lovell, M. R., Pillepich, A., Genel, S., et al. 2018, *MNRAS*, 481, 1950, doi: [10.1093/mnras/sty2339](https://doi.org/10.1093/mnras/sty2339)
- Ludlow, A. D., Schaye, J., Schaller, M., & Bower, R. 2020, *MNRAS*, 493, 2926, doi: [10.1093/mnras/staa316](https://doi.org/10.1093/mnras/staa316)
- Marinacci, F., Vogelsberger, M., Pakmor, R., et al. 2018, *MNRAS*, 480, 5113, doi: [10.1093/mnras/sty2206](https://doi.org/10.1093/mnras/sty2206)
- McKeown, D., Bullock, J. S., Mercado, F. J., et al. 2022, *MNRAS*, 513, 55, doi: [10.1093/mnras/stac966](https://doi.org/10.1093/mnras/stac966)
- Merritt, D., Graham, A. W., Moore, B., Diemand, J., & Terzić, B. 2006, *AJ*, 132, 2685, doi: [10.1086/508988](https://doi.org/10.1086/508988)
- Monaghan, J. J. 1992, *ARA&A*, 30, 543, doi: [10.1146/annurev.aa.30.090192.002551](https://doi.org/10.1146/annurev.aa.30.090192.002551)
- Mostow, O., Torrey, P., Rose, J. C., et al. 2024, arXiv e-prints, arXiv:2412.09566, doi: [10.48550/arXiv.2412.09566](https://doi.org/10.48550/arXiv.2412.09566)
- Muratov, A. L., Kereš, D., Faucher-Giguère, C.-A., et al. 2015, *MNRAS*, 454, 2691, doi: [10.1093/mnras/stv2126](https://doi.org/10.1093/mnras/stv2126)

- Naiman, J. P., Pillepich, A., Springel, V., et al. 2018, *MNRAS*, 477, 1206, doi: [10.1093/mnras/sty618](https://doi.org/10.1093/mnras/sty618)
- Navarro, J. F., Frenk, C. S., & White, S. D. M. 1997, *ApJ*, 490, 493, doi: [10.1086/304888](https://doi.org/10.1086/304888)
- Nelson, D., Pillepich, A., Springel, V., et al. 2018, *MNRAS*, 475, 624, doi: [10.1093/mnras/stx3040](https://doi.org/10.1093/mnras/stx3040)
- Nelson, D., Springel, V., Pillepich, A., et al. 2019a, *Computational Astrophysics and Cosmology*, 6, 2, doi: [10.1186/s40668-019-0028-x](https://doi.org/10.1186/s40668-019-0028-x)
- Nelson, D., Pillepich, A., Springel, V., et al. 2019b, *MNRAS*, 490, 3234, doi: [10.1093/mnras/stz2306](https://doi.org/10.1093/mnras/stz2306)
- Newman, A. B., Treu, T., Ellis, R. S., et al. 2013, *ApJ*, 765, 24, doi: [10.1088/0004-637X/765/1/24](https://doi.org/10.1088/0004-637X/765/1/24)
- Ni, Y., Genel, S., Anglés-Alcázar, D., et al. 2023, *ApJ*, 959, 136, doi: [10.3847/1538-4357/ad022a](https://doi.org/10.3847/1538-4357/ad022a)
- Oñorbe, J., Boylan-Kolchin, M., Bullock, J. S., et al. 2015, *MNRAS*, 454, 2092, doi: [10.1093/mnras/stv2072](https://doi.org/10.1093/mnras/stv2072)
- Oman, K. A., Navarro, J. F., Fattahi, A., et al. 2015, *MNRAS*, 452, 3650, doi: [10.1093/mnras/stv1504](https://doi.org/10.1093/mnras/stv1504)
- Ou, X., Eilers, A.-C., Necib, L., & Frebel, A. 2024, *MNRAS*, 528, 693, doi: [10.1093/mnras/stae034](https://doi.org/10.1093/mnras/stae034)
- Ou, X., Necib, L., Wetzel, A., et al. 2025, arXiv e-prints, arXiv:2503.05877, doi: [10.48550/arXiv.2503.05877](https://doi.org/10.48550/arXiv.2503.05877)
- Persic, M., Salucci, P., & Stel, F. 1996, *MNRAS*, 281, 27, doi: [10.1093/mnras/278.1.27](https://doi.org/10.1093/mnras/278.1.27)
- Pillepich, A., Springel, V., Nelson, D., et al. 2018a, *MNRAS*, 473, 4077, doi: [10.1093/mnras/stx2656](https://doi.org/10.1093/mnras/stx2656)
- Pillepich, A., Nelson, D., Hernquist, L., et al. 2018b, *MNRAS*, 475, 648, doi: [10.1093/mnras/stx3112](https://doi.org/10.1093/mnras/stx3112)
- Pillepich, A., Nelson, D., Springel, V., et al. 2019, *MNRAS*, 490, 3196, doi: [10.1093/mnras/stz2338](https://doi.org/10.1093/mnras/stz2338)
- Planck Collaboration, Ade, P. A. R., Aghanim, N., et al. 2014, *A&A*, 571, A16, doi: [10.1051/0004-6361/201321591](https://doi.org/10.1051/0004-6361/201321591)
- . 2016, *A&A*, 594, A13, doi: [10.1051/0004-6361/201525830](https://doi.org/10.1051/0004-6361/201525830)
- Pontzen, A., & Governato, F. 2012, *MNRAS*, 421, 3464, doi: [10.1111/j.1365-2966.2012.20571.x](https://doi.org/10.1111/j.1365-2966.2012.20571.x)
- Qi, J., Garcia, A. M., Torrey, P., et al. 2025, arXiv e-prints, arXiv:2501.18687, doi: [10.48550/arXiv.2501.18687](https://doi.org/10.48550/arXiv.2501.18687)
- Rey, M. P., Agertz, O., Starkenburg, T. K., et al. 2023, *MNRAS*, 521, 995, doi: [10.1093/mnras/stad513](https://doi.org/10.1093/mnras/stad513)
- Rose, J. C., Torrey, P., Vogelsberger, M., & O’Neil, S. 2023, *MNRAS*, 519, 5623, doi: [10.1093/mnras/stac3634](https://doi.org/10.1093/mnras/stac3634)
- Rose, J. C., Torrey, P., Villaescusa-Navarro, F., et al. 2025, *ApJ*, 982, 68, doi: [10.3847/1538-4357/ad8e5](https://doi.org/10.3847/1538-4357/ad8e5)
- Rubin, V. C., Ford, Jr., W. K., & Thonnard, N. 1980, *ApJ*, 238, 471, doi: [10.1086/158003](https://doi.org/10.1086/158003)
- Sales, L. V., Wetzel, A., & Fattahi, A. 2022, *Nature Astronomy*, 6, 897, doi: [10.1038/s41550-022-01689-w](https://doi.org/10.1038/s41550-022-01689-w)
- Schaller, M., Frenk, C. S., Bower, R. G., et al. 2015, *MNRAS*, 451, 1247, doi: [10.1093/mnras/stv1067](https://doi.org/10.1093/mnras/stv1067)
- Schaye, J., & Dalla Vecchia, C. 2008, *MNRAS*, 383, 1210, doi: [10.1111/j.1365-2966.2007.12639.x](https://doi.org/10.1111/j.1365-2966.2007.12639.x)
- Sobol’, I. M. 1967, *Zhurnal Vychislitel’noi Matematiki i Matematicheskoi Fiziki*, 7, 784
- Sofue, Y., & Rubin, V. 2001, *ARA&A*, 39, 137, doi: [10.1146/annurev.astro.39.1.137](https://doi.org/10.1146/annurev.astro.39.1.137)
- Somerville, R. S., & Davé, R. 2015, *ARA&A*, 53, 51, doi: [10.1146/annurev-astro-082812-140951](https://doi.org/10.1146/annurev-astro-082812-140951)
- Springel, V. 2010a, *MNRAS*, 401, 791, doi: [10.1111/j.1365-2966.2009.15715.x](https://doi.org/10.1111/j.1365-2966.2009.15715.x)
- . 2010b, *ARA&A*, 48, 391, doi: [10.1146/annurev-astro-081309-130914](https://doi.org/10.1146/annurev-astro-081309-130914)
- Springel, V., & Hernquist, L. 2003, *MNRAS*, 339, 289, doi: [10.1046/j.1365-8711.2003.06206.x](https://doi.org/10.1046/j.1365-8711.2003.06206.x)
- Springel, V., White, S. D. M., Jenkins, A., et al. 2005, *Nature*, 435, 629, doi: [10.1038/nature03597](https://doi.org/10.1038/nature03597)
- Springel, V., Pakmor, R., Pillepich, A., et al. 2018, *MNRAS*, 475, 676, doi: [10.1093/mnras/stx3304](https://doi.org/10.1093/mnras/stx3304)
- Torrey, P., Vogelsberger, M., Genel, S., et al. 2014, *MNRAS*, 438, 1985, doi: [10.1093/mnras/stt2295](https://doi.org/10.1093/mnras/stt2295)
- Velmani, P., & Paranjape, A. 2023, *MNRAS*, 520, 2867, doi: [10.1093/mnras/stad297](https://doi.org/10.1093/mnras/stad297)
- Villaescusa-Navarro, F., Wandelt, B. D., Anglés-Alcázar, D., et al. 2022, *ApJ*, 928, 44, doi: [10.3847/1538-4357/ac54a5](https://doi.org/10.3847/1538-4357/ac54a5)
- Villaescusa-Navarro, F., Anglés-Alcázar, D., Genel, S., et al. 2021, *ApJ*, 915, 71, doi: [10.3847/1538-4357/abf7ba](https://doi.org/10.3847/1538-4357/abf7ba)
- Virtanen, P., Gommers, R., Oliphant, T. E., et al. 2020, *Nature Methods*, 17, 261, doi: [10.1038/s41592-019-0686-2](https://doi.org/10.1038/s41592-019-0686-2)
- Vogelsberger, M., Marinacci, F., Torrey, P., & Puchwein, E. 2020, *Nature Reviews Physics*, 2, 42, doi: [10.1038/s42254-019-0127-2](https://doi.org/10.1038/s42254-019-0127-2)
- Walker, M. G., & Peñarrubia, J. 2011, *ApJ*, 742, 20, doi: [10.1088/0004-637X/742/1/20](https://doi.org/10.1088/0004-637X/742/1/20)
- Wang, W., Han, J., Cautun, M., Li, Z., & Ishigaki, M. N. 2020, *Science China Physics, Mechanics, and Astronomy*, 63, 109801, doi: [10.1007/s11433-019-1541-6](https://doi.org/10.1007/s11433-019-1541-6)
- Wang, Y., Nadler, E. O., Mao, Y.-Y., et al. 2024, *ApJ*, 976, 119, doi: [10.3847/1538-4357/ad7f4c](https://doi.org/10.3847/1538-4357/ad7f4c)
- Weinberger, R., Springel, V., Hernquist, L., et al. 2017, *MNRAS*, 465, 3291, doi: [10.1093/mnras/stw2944](https://doi.org/10.1093/mnras/stw2944)
- Weinberger, R., Springel, V., Pakmor, R., et al. 2018, *MNRAS*, 479, 4056, doi: [10.1093/mnras/sty1733](https://doi.org/10.1093/mnras/sty1733)
- Zhang, X., Chen, B., Chen, P., Sun, J., & Tian, Z. 2024, *MNRAS*, 528, 2653, doi: [10.1093/mnras/stae025](https://doi.org/10.1093/mnras/stae025)
- Zhao, H. 1996, *MNRAS*, 278, 488, doi: [10.1093/mnras/278.2.488](https://doi.org/10.1093/mnras/278.2.488)